J Eng Math: (2022) 132:14
https://doi.org/10.1007/s10665-021-10191-7

The steady laminar planar mixing layer flow of viscoelastic FENE-P fluids

S. Parvar · C. B. da Silva · F. T. Pinho

Received: 28 April 2021 / Accepted: 7 November 2021

Abstract An approximate self-similar solution is proposed for the steady laminar mixing layer flow of viscoelastic fluids, described by the FENE-P constitutive equation. The solution is obtained by performing an order of magnitude analysis and ensuing simplifications of the governing equations following the procedures used in the corresponding planar boundary layer flow solution (Parvar S, Silva CB, Pinho FT, Phys Fluids 33(2):023103, 2021). The effects of Weissenberg number, maximum polymer extensibility and viscosity ratio on mixing layer, displacement, and momentum thicknesses as well as on velocity, stress, and conformation tensor profiles are investigated in detail. At low elasticity levels, the mixing layer exhibits a self-similar behavior, with the kinematic quantities collapsing on the corresponding Newtonian flow curves and the polymer characteristics exhibiting a unique behavior if adequately normalized. However, with increasing levels of elasticity not only the profiles deviate from the low elasticity levels asymptote, but they cease to collapse onto single curves, showing a dependence on local values of the relevant dimensionless numbers, i.e., the approximate similar solution becomes local. Our solution matches the corresponding Newtonian solution and compares well with the significantly costlier numerical simulations using the RheoFoam toolbox of OpenFoam open-source code.

Keywords Local approximate self-similar solution · Free shear flow · Mixing layer flow · Viscoelastic fluid · FENE-P model

1 Introduction

The mixing layer flow is one of three canonical wall-free shear flows (others being the free jet and the wake), which are immensely relevant to our understanding of modern fluid mechanics precisely for being present (at least in part) in virtually all natural and industrial flows. One cannot overstate the importance of these canonical flows, from which the mixing layer case addressed here is probably the simplest of all the configurations. Indeed, it is fair to say

F. T. Pinho · S. Parvar
CEFT/FEUP, Universidade do Porto, Rua Dr. Roberto Frias, 4200-465 Porto, Portugal
e-mail: s.parvar@hotmail.com

S. Parvar (✉)
INEGI, Campus da FEUP, Rua Dr. Roberto Frias, 4200-465 Porto, Portugal

C. B. da Silva
LAETA, IDMEC, Instituto Superior Técnico, Universidade de Lisboa, Lisbon, Portugal

Published online: 31 December 2021

that much of the insights we are able to gain when analyzing complex fluid mechanics problems actually arise from our knowledge of this class of very simple canonical flows. The fact that the mixing layer configuration is probably the simplest of all the canonical flows explains its great importance since mixing layers arise from regions with strong velocity differences which exist in virtually all flows, e.g., the initial region of a planar jet can be described by the evolution of two, opposite, mixing layers. Even though steady mixing layer flows are today reasonably well understood for Newtonian fluids, both in the laminar [1,2] and turbulent regimes [3], there is presently no known solution for the corresponding steady laminar flow case with viscoelastic fluids, as shown in the review below. Of particular interest are cases allowing analytical or semi-analytical solutions, as is the case with similarity solutions, as these provide a clearer picture of all the effects of the independent dimensionless numbers onto the flow characteristics in addition to being less expensive to obtain than full numerical solutions, as is clear from classical fluid mechanics [1,2].

In particular, the approximate self-similar solution of the viscoelastic steady laminar mixing layer flow obtained in this work will be useful as a benchmark for the verification of numerical tools to deal with the corresponding laminar and especially turbulent flows, and it will provide quantitative information and insight onto the laminar flow characteristics for low and intermediate levels of elasticity.

The boundary layer theory of Prandtl [4] allowed the approximate similarity solution of the planar boundary layer flow by Blasius [5], and those ideas and methods were subsequently applied to wall and wall-free shear flows (the 2D wake flow is actually self-similar without the need to invoke the boundary layer approximation as reported by Birkhoff and Zarantonello [6]). The simplified governing equations, benefitting from boundary layer approximations and written in terms of similarity variables, are the same for boundary and mixing layer flows, each obeying specific boundary conditions. For the laminar steady flow between parallel streams, or laminar mixing layer flow, Lessen [7] and Chapman [8] were among the first to obtain the approximate solution, the former for incompressible fluids, the latter for compressible fluids, but including the incompressible case as a limit case. Lessen [7] investigated the stability of the mixing layer flow, following Kuethe and Von Kármán [9] by assuming the velocity profiles to be continuous functions in the streamwise and normal directions, but they neither presented profiles nor the corresponding numerical values, and only indicated how they could be obtained. In contrast, Chapman [8] presented profiles at various Mach numbers, including the incompressible flow case (zero Mach number). Tabulated data were listed by Lock [10], who provided the full solution through an extension of Lessen's work to parallel streams of fluids with different properties. Other developments considered the case of a non-uniform velocity stream of incompressible fluid meeting fluid at rest by Nash [11], while both Ting [12] and Klemp and Acrivos [13] further extended the compressible Newtonian mixing layer flow analysis.

For generality, the search for full self-similar solutions, i.e., without invoking approximations, was sometimes carried out with generalized Newtonian fluids, where the viscosity function is described by a power law, as reported in Birkhoff and Zarantonello [6] and explained more recently by Voropayev et al. [14].

Although laminar Newtonian mixing layer flows have been investigated extensively, for the corresponding non-Newtonian flows the literature is scarcer, in particular when fluids are viscoelastic. For the large Reynolds number flows of interest to this work the focus has been essentially on the effects of viscoelasticity in the development of flow instabilities that ultimately lead to a transition from laminar to turbulent flow. Azaiez and Homsy [15] performed a linear stability analysis with different viscoelastic models (Oldroyd-B, corotational Jeffreys, and Giesekus models) and especially aimed at the inviscid modes. They showed that in this limit fluid elasticity reduces instability but does not suppress it provided the elasticity number is finite (they also reported that if the Weissenberg number tends to infinity in such a way that the elasticity number (El) increases then the maximum growth rate of the perturbations and corresponding wavenumbers vary as $\propto 1/El$). This stabilization mechanism was explained in the corresponding Appendix E, authored by Hinch [16], as being equivalent to that due to an elastic membrane. Azaiez and Homsy further investigated the effects of viscoelasticity in [17] through several temporal and two-dimensional numerical simulations with both Oldroyd-B and FENE-P fluid models (FENE-P stands for "Finitely Extensible Non-linear Elastic" model with Peterlin's closure [18–20]). For the Oldroyd-B fluid the instabilities were associated with the model deficiency in allowing unbounded growth of elastic stresses, ultimately leading to the code divergence (a good example of the so-called high Weissenberg number problem). For the FENE-P model they reported that viscoelastic

effects were negligible on the global vortex structure and the roll-up and pairing times of the vortex, but nevertheless noticed more concentrated vorticity at spots of higher elastic normal stresses in the braids and in the vortex core regions, with vortex structures lasting longer than for Newtonian fluids. Kumar and Homsy [21] carried out further investigations of hydrodynamic instabilities on the onset of turbulence through direct numerical simulations (DNS) of free shear layer flows of FENE-P fluids. They found that for sufficiently high polymer extensibility and relaxation time the roll-up process is inhibited while large polymer stress gradients develop.

In the numerical investigations of viscoelasticity effects upon coherent structures in mixing layer flow of FENE-P fluids by Yu and Phan-Thien [22], artificial diffusion was used and this inhibited numerical instabilities. They observed that the growth of polymer normal stress differences attenuated several types of large-scale structures, which also had an impact on the suppression of small-scale structures. Ray and Zaki [23] looked at the absolute instability for the Oldroyd-B and FENE-P models and found elasticity to be destabilizing for the Oldroyd-B model and stabilizing for the FENE-P model except when the maximum dumbbell extensibility is very large (i.e., when the FENE-P tends to the Oldroyd-B model). Under creeping flow conditions there are instabilities of purely elastic nature that have recently been experimentally investigated by Varshney and Steinberg [24]. Therefore, under conditions of large flow elasticity and for large Reynolds numbers in which the flow transitions to turbulent, there is a wealth of behavior over the whole range of Reynolds number.

This work aims to present the stable steady viscoelastic solution for the high Reynolds number laminar mixing layer flow of viscoelastic fluids, here described by the FENE-P model, but below the conditions leading to laminar–turbulent transition. As also discussed in the previous works who used this model, this is a suitable constitutive equation for the rheology of dilute polymer solutions that is of interest to this work. Prior to that we quickly review the literature regarding the related cases of stable laminar boundary layer and jet flows of viscoelastic fluids. Rajagopal et al. [25] investigated Falkner–Skan flows of second-order fluids and reported that similarity not only required a large Reynolds number (Re), but also $\mathrm{Re}/Wi \gg 1$, where Wi is the Weissenberg number defined as the ratio of elastic over viscous forces. Olagunju [26,27] obtained a local approximate similarity solution for the boundary layer flow over a flat plate of viscoelastic fluids described by the FENE-P, because it remained dependent on the streamwise coordinate through the FENE-P equation. This contrasts with the global nature of the approximate self-similar solution of Newtonian flows [5]. Subsequently, while studying the laminar planar jet [28,29] and boundary layer [30] flows of FENE-P fluids, Parvar et al. [28,30] noticed that Olagunju had ignored some terms in his elastic stress equations. Although their impact on the velocity profiles was weak, they lead to inaccurate predictions of the polymer stresses. This paper is an extension to the mixing layer flow of the approximate theory used in the investigations of the laminar planar jet [28,29] and boundary layer flows of FENE-P fluids [30].

This text is organized as follows: after presenting the flow set-up, the coordinate system and the full set of governing equations, we explain in Sect. 3 the simplifications leading to the final simplified differential momentum equation and the algebraic cubic equations for the conformation tensor components. This set is identical to that for the boundary layer flow, but the boundary conditions are different. The numerical methods used to solve them are given in Sect. 4 and their results and the corresponding discussion are the subject of Sect. 5.

2 Flow problem and governing equations

The schematic of laminar mixing layer flow is shown in Fig. 1: two parallel streams with different uniform velocities U_1 and U_2 ($U_1 > U_2$) meet at $x = 0$, downstream a very thin frictionless plate called splitter plate (present at $x < 0$). The interacting streams form the mixing layer, and the transverse coordinate is y. Momentum diffusion smoothens the velocity discontinuity and at some distance downstream the plate trailing edge the flow characteristics no longer depend on the plate existence. For high enough Reynolds numbers, the thin boundary layer approximations are valid in the mixing layer flow [1,2]. Since the two parallel streams remain uniform and constant far from the mixing layer, the streamwise pressure gradient is null ($\partial p/\partial x = 0$) in the free-stream flows. The mixing layer thickness (δ) is defined as in Pope [3], but in laminar flow it is more common to use a 1% rather than a 5% criterion. This thickness is the distance between the locations y_α with local velocity U_α, with $\alpha = 0.01$ and 0.99, i.e., $\delta = y_{0.99} - y_{0.01}$,

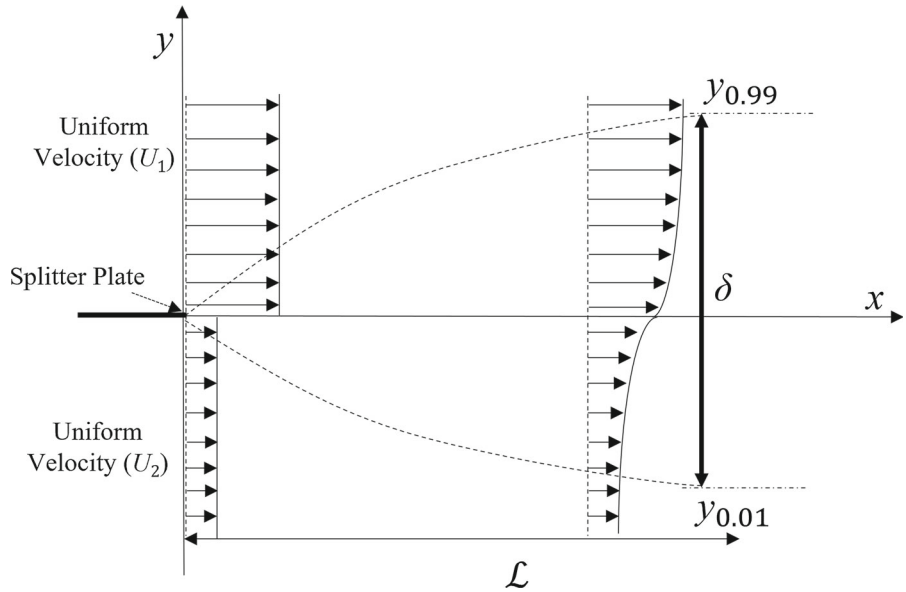

Fig. 1 The schematics of the mixing layer flow and definition of the mixing layer thickness and coordinate system. (The splitter plate is present at $x < 0$) The z-coordinate is normal to the plane

where U_α is given as

$$U_\alpha = U_2 + \alpha(U_1 - U_2), \tag{1}$$

with U_1 and U_2 denoting the large and small free-stream velocities, respectively (cf. Fig. 1). These flow conditions define two characteristic velocities, the difference between the free-stream velocities and their average value: by using these to define a dimensionless velocity profile the shear layer thickness corresponds to the distance between the locations where the dimensionless velocities differ by 1% from the free-stream values.

The viscoelastic fluid is described by the finitely extensible non-linear elastic model with Peterlin's closure (FENE-P) [20,31], which has the ingredients required to capture the main features of viscoelasticity in dilute polymer solutions, such as memory effects, shear-thinning behavior, and bounded elastic stresses.

The governing equations are presented next in indicial notation. The conservation of mass for incompressible fluids is

$$\frac{\partial u_k}{\partial x_k} = 0, \tag{2}$$

and the Cauchy equation is written as

$$\rho\left(\frac{\partial u_i}{\partial t} + u_k\frac{\partial u_i}{\partial x_k}\right) = -\frac{\partial P}{\partial x_i} + \frac{\partial \tau_{ik}}{\partial x_k}, \tag{3}$$

where u_i is the velocity vector, P is the pressure, and ρ is the fluid density. The fluid extra stress τ_{ij} is given by

$$\tau_{ij} = \tau_{ij}^{\mathrm{s}} + \tau_{ij}^{\mathrm{p}}, \tag{4}$$

the sum of the Newtonian solvent stress (τ_{ij}^{s}) with the polymer stress (τ_{ij}^{p}). The Newtonian solvent stress tensor is written as

$$\tau_{ij}^{\mathrm{s}} = 2\rho\upsilon_{\mathrm{s}}S_{ij}, \tag{5}$$

where υ_{s} is its kinematic viscosity, and S_{ij} is the rate-of-strain tensor defined by

$$S_{ij} = \frac{1}{2}\left(\frac{\partial u_i}{\partial x_j} + \frac{\partial u_j}{\partial x_i}\right). \tag{6}$$

The polymer stress tensor is given by the FENE-P model, here written as

$$\tau_{ij}^{\mathrm{p}} = \frac{\rho \upsilon_{\mathrm{p}}}{\lambda}\left[f\left(C_{kk}\right) C_{ij} - f_{\mathrm{s}}(L)\delta_{ij}\right], \tag{7}$$

where υ_{p} is the zero-shear rate polymer kinematic viscosity coefficient, λ is the relaxation time, δ_{ij} is the identity tensor, C_{ij} is the dimensionless conformation tensor, and $f\left(C_{kk}\right)$ is the scalar Peterlin function. This function depends on the trace of the conformation tensor and on the square of the maximum normalized dumbbell extensibility (L^2) and $f_{\mathrm{s}}\left(L\right)$ is a second scalar function of L^2, that in several variants of the FENE-P model equals $f\left(C_{kk}\right)$ at equilibrium, i.e., at rest. There are several variants of the FENE-P model in the literature, however, by considering $L^2 \gg 3$ they essentially provide identical results. Three of those variants use

$$f\left(C_{kk}\right) = \frac{L^2}{L^2 - C_{kk}} \quad \text{and} \quad f_{\mathrm{s}}\left(L\right) = 1, \tag{8a}$$

$$f\left(C_{kk}\right) = \frac{L^2}{L^2 - C_{kk}} \quad \text{and} \quad f_{\mathrm{s}}\left(L\right) = \frac{L^2}{L^2 - 3}, \tag{8b}$$

$$f\left(C_{kk}\right) = \frac{L^2 - 3}{L^2 - C_{kk}} \quad \text{and} \quad f_{\mathrm{s}}\left(L\right) = 1. \tag{8c}$$

The first set of functions is the original, later Bird et al. [19] modified it to Eq. (8b) as discussed in Beris and Edwards [32]. Vaithianathan and Collins [33] were among the first who used the third variant, extensively used in investigations of turbulent flows of polymer solutions [34–38]. In this work, the mathematical formulations are general and independent of the set of functions, but the results presented are for the third variant (Eq. (8c)).

To close the polymer model, the conformation tensor is described by the following evolution equation:

$$\underbrace{\frac{\partial C_{ij}}{\partial t}}_{\text{temporal term}} + \underbrace{u_k \frac{\partial C_{ij}}{\partial x_k}}_{\text{advection term}} = \underbrace{C_{jk}\frac{\partial U_i}{\partial x_k} + C_{ik}\frac{\partial U_j}{\partial x_k}}_{\text{distortion term}} \underbrace{-\frac{1}{\lambda}[f(C_{kk})C_{ij} - f_{\mathrm{s}}(L)\delta_{ij}]}_{\text{relaxation term}}, \tag{9}$$

in which the first and second terms on the left-hand side express the local time variation and advection of the conformation tensor, respectively, whereas the first two terms and the last term on the right-hand side express its polymer distortion and relaxation, respectively.

3 Simplified governing equations

3.1 Momentum equations

The arguments used to simplify the governing equations for the mixing layer flows of FENE-P fluids are the same as for the boundary layer flow analysis of Parvar et al. [30], where more details can be found. Next, we briefly summarize them and then present the final set of simplified equations.

We introduce first the zero-shear rate kinematic viscosity(ν_0) given as the following sum of the solvent and polymer kinematic viscosities

$$\nu_0 = \nu_{\mathrm{s}} + \nu_{\mathrm{p}}, \tag{10}$$

and the ratio of viscosities (β_{p})

$$\beta_{\mathrm{p}} = \frac{\nu_{\mathrm{p}}}{\nu_{\mathrm{s}} + \nu_{\mathrm{p}}} = \frac{\nu_{\mathrm{p}}}{\nu_0}. \tag{11}$$

The Reynolds number ($\mathrm{Re}_{\mathcal{L}}$) is defined as

$$\mathrm{Re}_{\mathcal{L}} = \frac{U_1 \mathcal{L}}{\nu_0}, \tag{12}$$

and the Weissenberg number ($Wi_{\mathcal{L}}$) is

$$Wi_{\mathcal{L}} = \frac{\lambda U_1}{\mathcal{L}}, \tag{13}$$

where U_1 is the large free-stream velocity and $\mathcal{L}$ is the maximum flow distance measured from the trailing edge of the splitter plate (cf. Fig. 1). The local coordinate x will also be used later as characteristic length. We use here the standard procedure (cf. [1,2]) to carry out the order of magnitude analysis of the governing equations, bearing in mind that experimental evidence shows that at sufficiently high Reynolds numbers we have $\delta \ll \mathcal{L}$. The normalized lengths and velocities (denoted with *) are defined as follows:

$$x^* = \frac{x}{\mathcal{L}}, \quad y^* = \frac{y}{\delta}, \; u^* = \frac{u}{U_1}, v^* = \frac{v\mathcal{L}}{U_1\delta}, \quad p^* = \frac{P}{\rho U_1^2}. \tag{14}$$

The dimensionless continuity equation becomes

$$\frac{\partial u^*}{\partial x^*} + \frac{\partial v^*}{\partial y^*} = 0, \tag{15}$$

and the normalized x-momentum equation is rewritten as

$$u^*\frac{\partial u^*}{\partial x^*} + v^*\frac{\partial u^*}{\partial y^*} = -\frac{\partial P^*}{\partial x^*} + \frac{\left(1-\beta_{\mathrm{p}}\right)}{\mathrm{Re}_{\mathcal{L}}}\frac{\mathcal{L}^2}{\delta^2}\left(\frac{\delta^2}{\mathcal{L}^2}\frac{\partial^2 u^*}{\partial x^{*2}} + \frac{\partial^2 u^*}{\partial y^{*2}}\right) + \frac{\beta_{\mathrm{p}}}{Wi_{\mathcal{L}}\mathrm{Re}_{\mathcal{L}}}\frac{\mathcal{L}}{\delta}\left(\frac{\delta}{\mathcal{L}}\frac{\partial\left[f\left(C_{kk}\right)C_{xx}-1\right]}{\partial x^*} + \frac{\partial\left[f\left(C_{kk}\right)C_{xy}\right]}{\partial y^*}\right). \tag{16}$$

This equation is simplified considering that the streamwise stress gradients are negligible in comparison to the transverse stress gradients, i.e., $\partial\tau^{\mathrm{s}}_{xx}/\partial x \ll \partial\tau^{\mathrm{s}}_{xy}/\partial y$ as for a Newtonian fluid, and $\partial\tau^{\mathrm{p}}_{xx}/\partial x \ll \partial\tau^{\mathrm{p}}_{xy}/\partial y$. In short this simplification arises because generally $\tau^{\mathrm{s}}_{xx} \sim \tau^{\mathrm{s}}_{xy}$ for the flow conditions under investigation, while $\partial/\partial x \ll \partial/\partial y$, which largely follows from $\delta \ll \mathcal{L}$. By using this concept and by performing an order of magnitude analysis, we notice that

$$\frac{\left(1-\beta_{\mathrm{p}}\right)}{\mathrm{Re}_{\mathcal{L}}}\frac{\partial^2 u^*}{\partial x^{*2}} \ll \frac{\left(1-\beta_{\mathrm{p}}\right)}{\mathrm{Re}_{\mathcal{L}}}\left(\frac{\mathcal{L}}{\delta}\right)^2\frac{\partial^2 u^*}{\partial y^{*2}}$$

and

$$\frac{\beta_{\mathrm{p}}}{Wi_{\mathcal{L}}\mathrm{Re}_{\mathcal{L}}}\frac{\partial\left(\left[f\left(C_{kk}\right)C_{xx} - f_{\mathrm{s}}\left(L\right)\right]\right)}{\partial x^*} \ll \frac{\beta_{\mathrm{p}}}{Wi_{\mathcal{L}}\mathrm{Re}_{\mathcal{L}}}\left(\frac{\mathcal{L}}{\delta}\right)\frac{\partial\left(\left[f\left(C_{kk}\right)C_{xy}\right]\right)}{\partial y^*},$$

because $\mathcal{L}/\delta \gg 1$. Note also that under the low Weissenberg number flow conditions imposed below, $f\left(C_{kk}\right) \approx 1$, $C_{xx} \approx 1$.

As discussed by Olagunju [26,27] and Parvar et al. [28–30], to get a solution for the laminar mixing layer flow the streamwise pressure gradient needs to be determined and the leading coefficients of

$$\frac{\partial^2 u^*}{\partial y^{*2}} \quad \text{and} \quad \frac{\partial\left(\left[f\left(C_{kk}\right)C_{xy}\right]\right)}{\partial y^*}$$

must be of $O(1)$ in order for the polymer and solvent stress terms to be of the same order of magnitude. At high enough Reynolds numbers and for dilute solutions ($1-\beta_{\mathrm{p}} \sim 1$), we have from the leading coefficient of the solvent shear stress term

$$\frac{(\mathcal{L}/\delta)^2}{\mathrm{Re}_{\mathcal{L}}} = O\left(1\right) \rightarrow \delta = O\left(\mathcal{L}\mathrm{Re}_{\mathcal{L}}^{-\frac{1}{2}}\right) \rightarrow \frac{\delta}{\mathcal{L}} \approx \mathrm{Re}_{\mathcal{L}}^{-\frac{1}{2}}, \tag{17}$$

which shows the classical boundary layer proportionality. Then, from the leading coefficient of the polymer shear stress term

$$\frac{\beta_{\mathrm{p}}}{Wi_{\mathcal{L}}\mathrm{Re}_{\mathcal{L}}}\left(\frac{\mathcal{L}}{\delta}\right) = O\left(1\right) \text{ or } Wi_{\mathcal{L}} = O\left(\beta_{\mathrm{p}}\mathrm{Re}_{\mathcal{L}}^{-\frac{1}{2}}\right). \tag{18}$$

This result shows that the validity of this simplified equation requires the Weissenberg number to be low, since it is inversely proportional to the square root of the Reynolds number as found previously for the boundary layer [26,27] and jet flows [28–30], respectively. However, since the momentum equation retains both shear stress terms, the solution remains valid if one of them predominates over the other, i.e., values of $Wi_{\mathcal{L}}$, well beyond those of Eq. (18) are allowed provided the discarded normal stress gradient term also remains negligible, as will be discussed later.

To determine the streamwise pressure gradient, the order of magnitude analysis of the y-momentum equation is carried out, which shows that all terms depending on the velocity vector in the y-momentum equation are also of negligible magnitude. Note that τ_{yy}^{p} of the FENE-P fluids is also negligible (it is null in homogenous shear flow), consequently $\partial p/\partial y$ is negligible, implying that the pressure in the outside inviscid-like flow is impressed into the mixing layer. Since the free-stream flows are uniform and constant, $\partial p/\partial x = 0$ outside and inside the mixing layer, as for the corresponding Newtonian case and there is no need to solve the y-momentum equation.

It is now advantageous to proceed with the dimensional form of the x-momentum equation for the planar mixing layer flow, which, in its final simplified form, is written as

$$u\frac{\partial u}{\partial x} + v\frac{\partial u}{\partial y} = \upsilon_s\frac{\partial^2 u}{\partial y^2} + \frac{\upsilon_p}{\lambda}\frac{\partial\left(f\left(C_{kk}\right)C_{xy}\right)}{\partial y}. \tag{19}$$

For this 2D flow, continuity is immediately enforced by the introduction of the stream function ψ defined as

$$u = \frac{\partial\psi}{\partial y}, \quad v = -\frac{\partial\psi}{\partial x}. \tag{20}$$

Upon substitution onto the simplified x-momentum equation, the following form is obtained:

$$\left(\frac{\partial\psi}{\partial y}\right)\left(\frac{\partial^2\psi}{\partial x\partial y}\right) - \left(\frac{\partial\psi}{\partial x}\right)\left(\frac{\partial^2\psi}{\partial y^2}\right) = (1-\beta_p)\upsilon_0\left(\frac{\partial^3\psi}{\partial y^3}\right) + \frac{\beta_p\upsilon_0}{\lambda}\frac{\partial\left(f\left(C_{kk}\right)C_{xy}\right)}{\partial y}, \tag{21}$$

where the solvent and polymer shear stresses have also been substituted by their definitions in Eqs. (5) and (7). Therefore, to get a closed form solution, the variations of C_{xy} and $f\left(C_{kk}\right)$ from the conformation tensor equation are required.

3.2 Conformation tensor equations

For a steady flow, the temporal term in Eq. (9) is exactly null and for the mixing layer flow ($u \gg v$ and $\partial/\partial y \gg \partial/\partial x$) advection of C_{ij} is negligible and the distortion and stress terms are essentially in equilibrium (terms on the right-hand side of Eq. (9)), i.e.,

$$C_{jk}\frac{\partial u_i}{\partial x_k} + C_{ik}\frac{\partial u_j}{\partial x_k} = \frac{1}{\lambda}\left[\left(C_{kk}\right)C_{ij} - f_s\left(L\right)\delta_{ij}\right]. \tag{22}$$

Quantifying the velocities through the stream function, the simplified evolution equations for the non-zero components of the conformation tensor are rewritten as

$$-2\left(C_{xx}\frac{\partial^2\psi}{\partial x\partial y} + C_{xy}\frac{\partial^2\psi}{\partial y^2}\right) + \frac{1}{\lambda}\left[f\left(C_{kk}\right)C_{xx} - f_s\left(L\right)\right] = 0, \tag{23}$$

$$2\left(C_{yx}\frac{\partial^2\psi}{\partial x^2} + C_{yy}\frac{\partial^2\psi}{\partial x\partial y}\right) + \frac{1}{\lambda}\left[f\left(C_{kk}\right)C_{yy} - f_s\left(L\right)\right] = 0, \tag{24}$$

$$\frac{1}{\lambda}\left[f\left(C_{kk}\right)C_{zz} - f_s\left(L\right)\right] = 0, \tag{25}$$

$$-C_{yy}\frac{\partial^2\psi}{\partial y^2} + C_{xx}\frac{\partial^2\psi}{\partial x^2} + \frac{1}{\lambda}\left[f\left(C_{kk}\right)C_{xy}\right] = 0. \tag{26}$$

Considering $\partial\psi/\partial x \ll \partial\psi/\partial y$ and that at low Weissenberg numbers the normal components of the conformation tensor are much larger than the shear components (at rest $C_{xx} = C_{yy} = C_{zz} \wedge \left[C_{xx} = 1 \vee C_{xx} = L^2/\left(L^2+3\right)\right]$

and $C_{ij(i\neq j)} \cong$ to ensure the deviatoric stress tensor of Eq. (7) is null), the simplified evolution equations for the components of the conformation tensor are

$$-2\lambda C_{xx}\frac{\partial^2\psi}{\partial x\partial y} - 2\lambda C_{xy}\frac{\partial^2\psi}{\partial y^2} + f\left(C_{kk}\right)C_{xx} = f_s\left(L\right), \tag{27}$$

$$2\lambda C_{yy}\frac{\partial^2\psi}{\partial x\partial y} + f\left(C_{kk}\right)C_{yy} = f_s\left(L\right), \tag{28}$$

$$f\left(C_{kk}\right)C_{zz} = f_s\left(L\right), \tag{29}$$

$$-\lambda C_{yy}\frac{\partial^2\psi}{\partial y^2} + f\left(C_{kk}\right)C_{xy} = 0. \tag{30}$$

Further manipulation provides the following expressions:

$$C_{xx} = \frac{f_s\left(L\right) + 2\lambda C_{xy}\frac{\partial^2\psi}{\partial y^2}}{\left(f\left(C_{kk}\right) - 2\lambda\frac{\partial^2\psi}{\partial x\partial y}\right)} = f_s\left(L\right)\frac{f\left(C_{kk}\right)\left(2\lambda\frac{\partial^2\psi}{\partial x\partial y} + f\left(C_{kk}\right)\right) + 2\lambda^2\left(\frac{\partial^2\psi}{\partial y^2}\right)^2}{f\left(C_{kk}\right)\left(f\left(C_{kk}\right)^2 - \left(2\lambda\frac{\partial^2\psi}{\partial x\partial y}\right)^2\right)}, \tag{31}$$

$$C_{yy} = \frac{f_s\left(L\right)}{\left(2\lambda\frac{\partial^2\psi}{\partial x\partial y} + f\left(C_{kk}\right)\right)}, \tag{32}$$

$$C_{zz} = \frac{f_s\left(L\right)}{f\left(C_{kk}\right)}, \tag{33}$$

$$C_{xy} = \frac{\lambda C_{yy}\frac{\partial^2\psi}{\partial y^2}}{f\left(C_{kk}\right)} = \frac{\lambda f_s\left(L\right)\frac{\partial^2\psi}{\partial y^2}}{f\left(C_{kk}\right)\left(f\left(C_{kk}\right) + 2\lambda\frac{\partial^2\psi}{\partial x\partial y}\right)}. \tag{34}$$

We have now a set of coupled algebraic equations for the conformation tensor components (C_{ij}), which depend on the flow characteristics via the stream function, on other C_{ij} components and on its trace via the Peterlin function. The Peterlin function is calculated by Eqs. (8a), (8b), (8c) as discussed below. By considering the three normal components of the conformation tensor, the trace C_{kk} becomes

$$C_{kk} = f_s\left(L\right)\frac{3f\left(C_{kk}\right)^2 + 2\lambda^2\left(\frac{\partial^2\psi}{\partial y^2}\right)^2 - 4\lambda^2\left(\frac{\partial^2\psi}{\partial x\partial y}\right)^2}{f\left(C_{kk}\right)\left(f\left(C_{kk}\right)^2 - 4\lambda^2\left(\frac{\partial^2\psi}{\partial x\partial y}\right)^2\right)}. \tag{35}$$

In the following, the adequate similarity variables η and function $G(\eta, x)$ [1,2] are identical to those used for the boundary layer flow with a constant free-stream velocity, and given by

$$\eta = \sqrt{\frac{U_1}{2\nu_0}}\frac{y}{x^{1/2}}, \qquad G\left(\eta, x\right) = \frac{\psi}{\sqrt{2U_1\nu_0 x}}. \tag{36}$$

The flow streamwise and cross-stream velocity components are obtained from their definitions, as

$$u = U_1 G'\left(\eta, x\right), \tag{37}$$

$$v = \sqrt{\frac{\nu_0 U_1}{2x}}\left(\eta G'\left(\eta, x\right) - G\left(\eta, x\right)\right), \tag{38}$$

where derivatives of $G(\eta, x)$ in order to η are denoted with primes. Using the similarity variables defined in Eq. (36) to transform the partial differential momentum equation into an ODE, a similarity solution is obtained for Newtonian fluids in which the function $G(\eta)$ is only dependent on η [1,2]. However, Olangunju [26,27] and Parvar et al. [28–30] reported that such self-similar solutions do not exist for the corresponding viscoelastic fluid flows and the flow problem remains two-dimensional because $G\left(\eta, x\right)$ is dependent on both η and x, even if other combinations of variables are used to define η and G above. Olangunju [26,27] and Parvar et al. [28–30] also found that it is possible

to obtain a simplified solution if an additional assumption is imposed, that the streamwise variation of $G(\eta, x)$ at constant η is negligible, i.e., that $\left(\frac{\partial G}{\partial x}\right)_\eta \approx 0$. Therefore, in the quantification of

$$\left(\frac{\partial G}{\partial x}\right)_y = \left(\frac{\partial G}{\partial x}\right)_\eta + \left(\frac{\partial G}{\partial \eta}\right)_x \frac{\partial \eta}{\partial x} \cong \left(\frac{\partial G}{\partial \eta}\right)_x \frac{\partial \eta}{\partial x},$$

the first term on the right-hand side is ignored. For the jet and boundary layer flows investigated in [28–30], this assumption still provided an accurate description of the velocity fields, while allowing for significantly simpler equations [39–43]. Without this assumption, the complexity of the final simplified equations increases significantly, while providing a negligible benefit as we found in comparisons with the numerical simulation of the original full governing equations. For conciseness, such comparison is not shown.

As shown by Olagunju [26,27] and Parvar et al. [28,30], it is through the Peterlin function equation, transformed by the use of the similarity variables, that one concludes about the dependence on both η and x. Renaming the Peterlin function as $K(\eta, x)$

$$K(\eta, x) = f(C_{kk}), \tag{39}$$

any of the Peterlin functions in Eqs. (8a), (8b), (8c) leads to the following third-order algebraic equation:

$$K^3 + \mathrm{C}_0 K^2 - Wi_x^2 \left(\eta G''\right)^2 K + \mathrm{C}_1 G''^2 + \mathrm{C}_2 \left(\eta G''\right)^2 = 0 \tag{40}$$

with dimensionless coefficients

$$\begin{aligned} C_0 &= \left(\frac{3I - 3f_s(L) - L^2}{L^2}\right), \\ \mathrm{C}_1 &= -\frac{\lambda^2 f_s(L) U_1^3}{\nu_0 L^2} x^{-1} = -\frac{f_s(L) \mathrm{Re}_x Wi_x^2}{L^2}, \\ C_2 &= \frac{\lambda^2 \left(L^2 + f_s(L) - 3I\right) U_1^2}{L^2} x^{-2} = \frac{\left(L^2 + f_s(L) - 3I\right) Wi_x^2}{L^2}, \end{aligned} \tag{41}$$

where $I = 1$ for the Peterlin function of Eq. (8c), and $I = 0$ for (8a) and (8b). These coefficients rely on the so-called local Reynolds and Weissenberg numbers, Re_x and Wi_x, respectively, defined in Eqs. (12) and (13)with x taking the place of $\mathcal{L}$ (x is the streamwise distance from the trailing edge of the splitter plate). It is the dependence on x of this set of coefficients C_1 and C_2 that tells us that the algebraic equation (40) depends on both η and x, and that the solution of the set of governing equations does not provide a global approximate self-similar solution as for Newtonian fluids, but instead a local approximate self-similar solution.

The remaining steps are now straightforward: back substituting C_{xy} from Eq. (34) into the simplified momentum equation (10) and casting it in terms of the similarity variables, we get

$$-GG'' = (1 - \beta_p) G''' + \beta_p f_s(L) \left(\frac{Wi_x G''^2 + K G''' - K' G''}{\left(K - Wi_x \eta G''\right)^2}\right). \tag{42}$$

This equation also depends on both x and η through the conformation tensor quantities and the first derivative of K relative to η, which is obtained from Eq. (40) and is given by

$$K' = -\frac{\left(2C_3\left(C_2 - Wi_x^2 K\right) + 2G'' G'''\left(C_1 + \eta^2\left(C_2 - Wi_x^2 K\right)\right)\right)}{C_4} \tag{43}$$

with

$$\begin{aligned} C_3 &= \eta G''^2, \\ C_4 &= \left(3K^2 + 2C_0 K - Wi_x^2 \left(\eta G''\right)^2\right). \end{aligned} \tag{44}$$

By substituting K' of Eq. (43) into Eq. (42) and further mathematical manipulation, the final format of the momentum equation is

$$G''' = -\frac{GG'' + \beta_p f_s(L) G'' \frac{\left(Wi_x C_4 G'' + 2C_3\left(C_2 - Wi_x^2 K\right)\right)}{\left(K - Wi_x \eta G''\right)^2 C_4}}{\left(\left(1-\beta_p\right) + \beta_p f_s(L) \frac{\left(C_4 K + 2G''^2\left(C_1 + \eta^2\left(C_2 - Wi_x^2 K\right)\right)\right)}{\left(K - Wi_x \eta G''\right)^2 C_4}\right)}. \tag{45}$$

4 Numerical solution

The simplified governing equations are a third-order differential equation on $G(\eta, x)$ and an algebraic cubic equation for $K(\eta, x)$. For their numerical solution, the third-order differential equation is converted to a system of first-order differential equations by considering the transformations, $G_1 = \frac{d^2G}{d\eta^2}$, $G_2 = \frac{dG}{d\eta}$, and $G_3 = G$.

First, the Cardan–Tartaglia formula [44] provides the real solution of the cubic algebraic equation. This solution must be physically correct, i.e., the normal components of the conformation tensor must be positive, and its trace bounded by 3 (the value at rest) and the square of the maximum dumbbell extensibility (L^2). Then, the system of differential equations is numerically solved with a fourth-order Runge–Kutta procedure coupled with a shooting method to apply the boundary conditions [45,46]. The free-stream velocity ratio (γ) is defined as

$$\gamma = \frac{U_2}{U_1}. \tag{46}$$

For the numerical solution of equations (40) and (45), three boundary conditions are required. Two of them consist on the top and bottom free-stream velocities, as in Eq. (40), and allow the accurate prediction of the shape of the velocity profile which, however, is not unique because it can shift in the transverse direction.

$$G'(+\infty) \to 1, \qquad G'(-\infty) \to \gamma. \tag{47}$$

These boundary conditions at infinity are essentially verified at $\eta = \pm 10$ for $\gamma = 0.5$ as discussed below (for lower values of γ a larger domain is required).

With the above set of conditions the semi-analytical solution of G is not fixed in space, i.e., it is not unique. In order to fix the solution, a third boundary condition is required as found previously [12,13,47]. This third boundary condition pins the solution into a unique profile for the mixing layer flow and in this procedure we follow Lock [10] and White [1], who suggested using

$$G(\eta = 0) = 0. \tag{48}$$

This condition is implemented as follows: an iterative procedure is used to find the place where $G = 0$, then the solution is shifted to the origin ($\eta = 0$). Typically, this is repeated 5 to 6 times until the origin stops shifting. Note that $G = 0$ also marks the inflection point, so the horizontal line downstream of the splitter plate ($\eta = y = 0$) is the centerline and connects inflection points.

5 Results and discussion

The semi-analytical solution is valid also for Newtonian fluids and this is verified through a comparison with Lock's solution and against the numerical simulation of the full set of governing equations. The latter are also used to check the upper limit of validity of the semi-analytical approximate similarity solution for the FENE-P fluid since its simplifications are not necessarily valid for all flow conditions in terms of flow elasticity. All the numerical simulations were carried out using the RheoFoam toolbox of the open-source code OpenFoam, and before we present results, we provide here information on the numerical method, flow domain, and meshes used.

Table 1 Characteristics of the meshes used in the RheoFoam calculations. The values of Δx and Δy are at the cells nearest the wall

Block	N_x	N_y	f_x	f_y	$\frac{\Delta x_{x=0}}{\delta_{x=\mathcal{L}}}$, $\frac{\Delta y_{x=0}}{\delta_{x=\mathcal{L}}}$	$\frac{\Delta x_{x=\mathcal{L}}}{\delta_{x=\mathcal{L}}}$
I&II	200	500	1.015	1.0092	0.0337, 0.0026	0.185

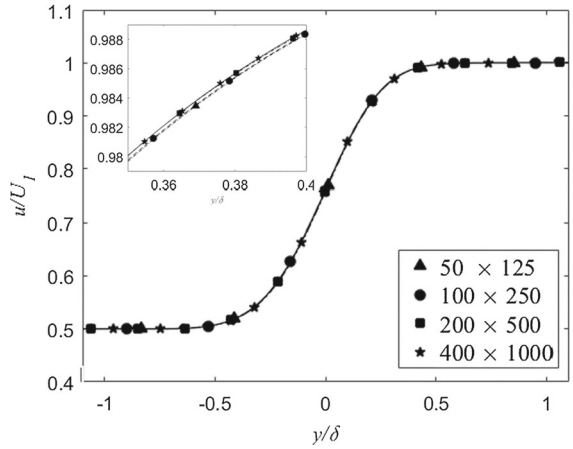

Fig. 2 Profiles of u/U_1 versus y/δ at for a self-similar Newtonian mixing layer flow at $\mathrm{Re}_x = 2000$ as obtained from Rheofoam simulations with four different meshes. The lines are a guide to the eye

OpenFoam is a finite volume code and the RheoFoam toolbox implements viscoelastic constitutive equations. It uses the high-order resolution scheme CUBISTA [48,49] to describe the advective terms in the momentum and conformation equations, diffusion terms are discretized with central differences and pressure–velocity coupling relies on the SIMPLEC algorithm [50]. The computational domain for this flow had a length $\mathcal{L}$, divided into two identical blocks, I and II on the positive and negative sides of y-axis. The width of each block was $2\mathcal{L}$ so the total width of the domain was $4\mathcal{L}$. Within each block a non-uniform computational grid had $N_x \times N_y$ cells in the x, y directions, respectively, as given in Table 1 together with the expansion/contraction mesh factors $f_x = \Delta_x^{i+1}/\Delta_x^i$ and $f_y = \Delta_y^{i+1}/\Delta_y^i$ and ratios of mesh size over mixing layer thickness at some locations. Mesh 200×500 was selected after an assessment of mesh independence using four grids with 50×125, 100×250, 200×500, and 400×1000 computational cells, in the x and y directions of the Newtonian mixing layer flow, respectively, as shown in Fig. 2. Differences between the results of grid 200×500 and those from a grid with twice the number of cells in each direction was below 0.005%.

At the inlet boundary uniform velocities were imposed ($U_1 = 1.0$ for block I and $U_2 = 0.5$ for block II) and a zero gradient condition was set for all other quantities. On the outlet boundary, the pressure was fixed to a constant value and a zero gradient condition was set for all other quantities. At the top boundary of block I and bottom boundary of block II, far from the mixing layer, the corresponding free-stream velocities were set.

The Newtonian simulation was carried out for $\gamma = 0.5$ and the results with the four meshes pertain to $x/\mathcal{L} = 0.2$, where the local Reynolds number is $\mathrm{Re}_x = 2 \times 10^3$. It is worth to mention that we noticed the results are dependent on initial conditions only for $x/\mathcal{L} < 0.2$ (because of the splitter plate), therefore our comparisons are carried out for $x/\mathcal{L} \geq 0.2$.

5.1 Verification: Newtonian fluids

Setting $\beta_\mathrm{p} = 0$, the governing equations for the viscoelastic fluid reduce to those for a Newtonian mixing layer flow which is used to verify the present solution [1]. Through asymptotic analysis, we found that infinity conditions are already achieved at $\eta = \pm 10$ for $\gamma = 0.5$, so the same conditions are considered here. It is worth mentioning that to choose an adequate Reynolds number, two conditions should be satisfied: (1) the Reynolds number should

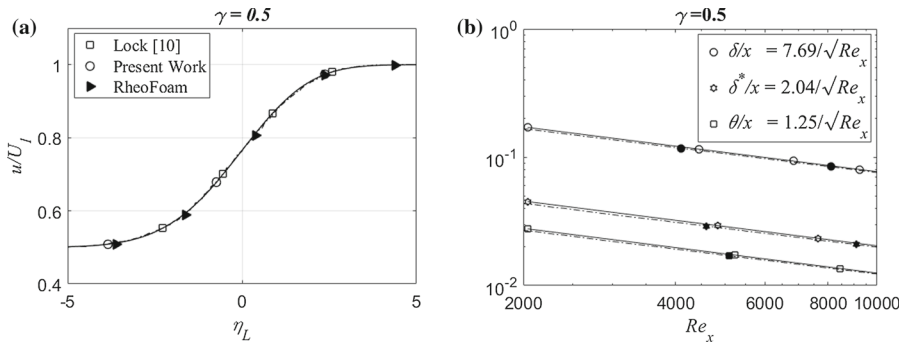

Fig. 3 Characteristics of the steady laminar mixing layer flow of Newtonian fluids in the self-similar region for $\gamma = 0.5$: **a** profiles of u/U_1 versus y/δ at $\mathrm{Re}_x = 2000$ and comparison with the literature [10] and Rheofoam results; **b** variation of δ/x, δ^*/x, and θ/x with Re_x and comparison with Rheofoam results (filled markers)

be high enough for the thin layer approximations to be valid [1] and (2) it should be below the critical condition for laminar–turbulent transition. As explained by Dimotakis [51], the critical Reynolds number for this transition is 1×10^4, if based on the mixing layer thickness (δ). Therefore, the maximum Reynolds number considered in the present study is $\mathrm{Re}_\delta = \frac{U_1\delta}{\nu_0} = 1\times 10^3$. It is also worth mentioning that in this paper, the Reynolds number at the maximum distance from the trailing edge of the splitter plate, denoted $\mathrm{Re}_{\mathcal{L}}$ (Eq. (12)), is also used for data normalization purposes.

Using $\gamma = 0.5$, Fig. 3a plots transverse profiles of velocity for Newtonian fluids, normalized by the upper free-stream velocity (U_1) and as a function of the similarity variable. It shows excellent agreement between the computed profiles of Eq. (37) and with both the solution of Lock [10] (note that Lock used a different definition of η ($\eta_L = \sqrt{\frac{U_1}{\nu_0}}\frac{y}{x^{1/2}}$)) and the numerical RheoFoam results.

The streamwise variation of global characteristics of the laminar mixing layer flow are plotted in Fig. 3b and also compared well with RheoFoam results. They are the mixing layer thickness (δ), defined in Eq. (1), the displacement thickness (δ^*) defined in

$$\delta^* = \int_{-\infty}^{+\infty}\left(1-\frac{u}{U_1}\right)\mathrm{d}y = \left(\int_{-\infty}^{0}\left(1-\frac{u}{U_1}\right)\mathrm{d}y + \int_{0}^{+\infty}\left(1-\frac{u}{U_1}\right)\mathrm{d}y\right), \tag{49}$$

and the momentum thickness (θ) given by

$$\theta = \int_{-\infty}^{+\infty}\frac{u}{U_1}\left(1-\frac{u}{U_1}\right)\mathrm{d}y = \left(\int_{-\infty}^{0}\frac{u}{U_1}\left(1-\frac{u}{U_1}\right)\mathrm{d}y + \int_{0}^{+\infty}\frac{u}{U_1}\left(1-\frac{u}{U_1}\right)\mathrm{d}y\right). \tag{50}$$

From our semi-analytical solution, and for $\gamma = 0.5$, the following relations were found for the three characteristic thicknesses:

$$\frac{\delta}{x} = \frac{7.69}{\sqrt{\mathrm{Re}_x}}, \quad \frac{\delta^*}{x} = \frac{2.04}{\sqrt{\mathrm{Re}_x}}, \quad \text{and} \quad \frac{\theta}{x} = \frac{1.25}{\sqrt{\mathrm{Re}_x}}.$$

From the latter two quantities, a shape factor ($H \equiv \delta^*/\theta$) of 1.633 was obtained. It is worth mentioning that we could not find in the cited Newtonian literature [1,2,10] any of these expressions. However, from the velocity profile extracted from Lock [10], we could calculate

$$\frac{\delta_L}{x} = \frac{7.68}{\sqrt{\mathrm{Re}_x}}, \quad \frac{\delta_L^*}{x} = \frac{2.08}{\sqrt{\mathrm{Re}_x}}, \quad \text{and} \quad \frac{\theta_L^*}{x} = \frac{1.28}{\sqrt{\mathrm{Re}_x}},$$

which are very close to our results.

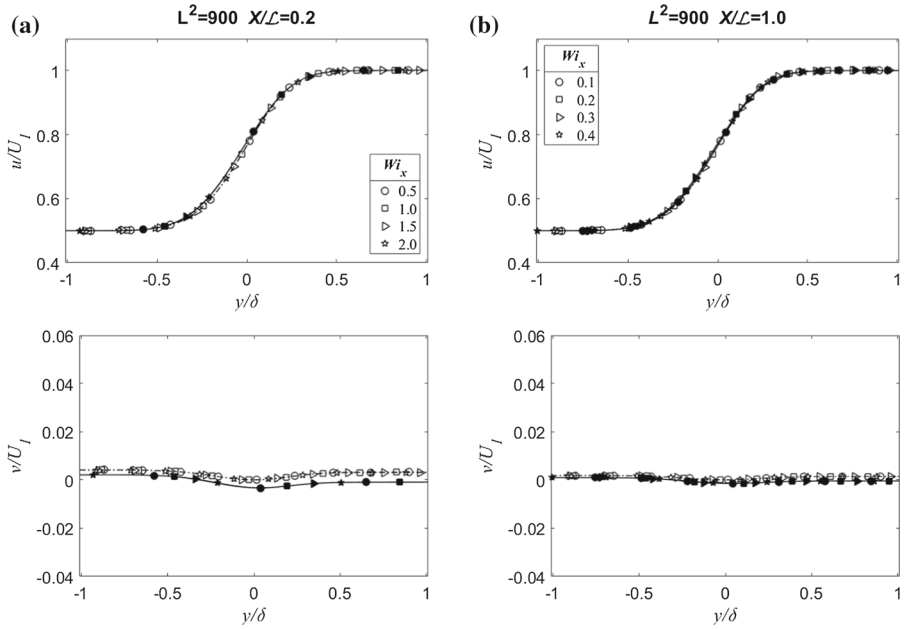

Fig. 4 Comparison between normalized transverse velocity profiles u/U_1 and v/U_1 for $\beta_p = 0.1$, $L^2 = 900$, $Re_x = 2 \times 10^4$ and 1×10^4 from the present solution (dash dotted lines and open symbols) and RheoFoam simulations (solid lines and closed symbols) at **a** $x/\mathcal{L} = 0.2$ and **b** $x/\mathcal{L} = 1$

5.2 FENE-P fluids

In this section, only the third set of Peterlin functions $f(C_{kk})$ and $f_s(L)$ of Eq. (8c) is used to obtain the numerical results. We keep the ratio of free-stream velocities constant at $\gamma = 0.5$ and the local Weissenberg number $Wi_x = \frac{\lambda U_1}{x}$ (defined in Eq. (13) with x instead of $\mathcal{L}$) is also used to present results.

5.2.1 Verification of FENE-P fluids

The simulation was carried out for the Peterlin function of Eq. (8c) with $\beta_p = 0.1$ and $L^2 = 900$ and the results shown pertain to $x/\mathcal{L} = 0.2$ and 1.0, where the local Reynolds numbers are $\mathrm{Re}_x = 2 \times 10^3$ and 1×10^4, and the Weissenberg numbers are in the range $0.5 \leq Wi_x \leq 2$ and $0.1 \leq Wi_x \leq 0.4$.

The transverse profiles of normalized streamwise velocities plotted in Fig. 4 show an excellent agreement with the RheoFoam data at both locations. Although the profiles of cross-stream velocity show a weak discrepancy at $x/\mathcal{L} = 0.2$, these values are less than 1% of the largest free-stream velocity and there is also good agreement between the results at $x/\mathcal{L} = 1$. Comparisons of velocity profiles for larger $Wi_x = 1$ are still very good but are not shown here for conciseness.

Figure 5a and b shows contours of the trace of the conformation tensor, which is proportional to the extension of the polymer molecules, for two cases with $Wi_{\mathcal{L}} = 0.2$ and $Wi_{\mathcal{L}} = 0.4$, respectively. The maxima C_{kk} happen where strain rates are the largest, which is along the inflection points of the velocity profiles. As expected, the values of C_{kk} decrease considerably on moving towards the free-stream flows, where the polymer dumbbells are not being stretched and the shear rates are null. The values of C_{kk} also decrease on moving downstream as elasticity effects decrease and increase when elasticity increases. In numerical simulations and in experiments, the line of maxima C_{kk} tends to have a slight inclination towards the low free-stream flow, as shown here [12,13,47], but as explained in Sect. 4, the semi-analytical solution fixes the inflection point at $y = 0$. Otherwise the shapes are all identical to those of the semi-analytical solution.

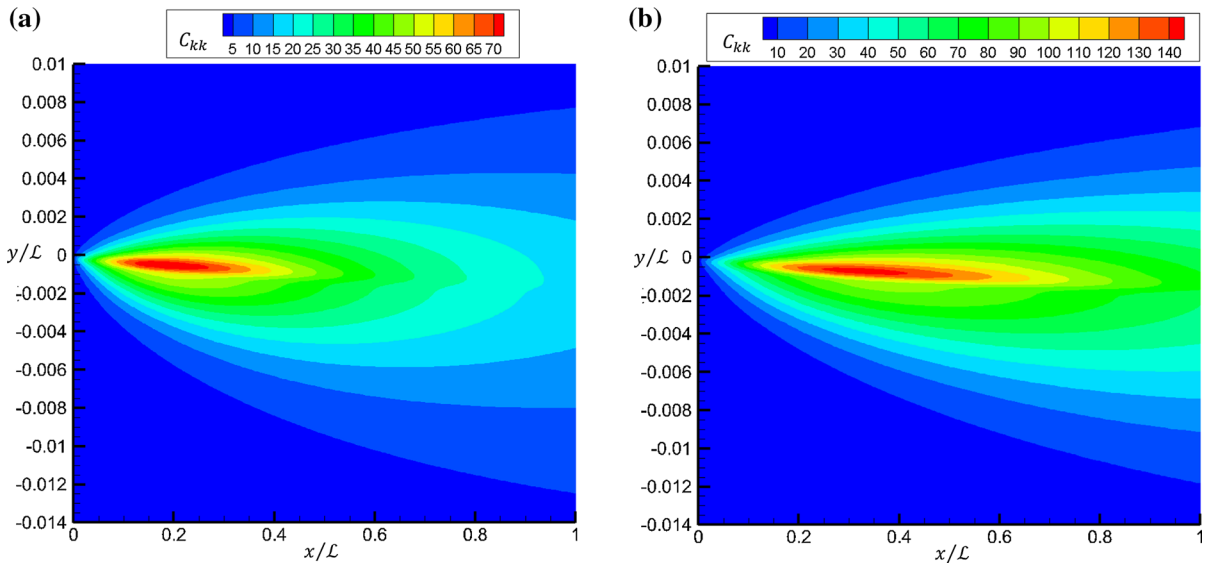

Fig. 5 Contours of the trace of the conformation tensor components C_{kk} from RheoFoam simulations with $\beta_p = 0.1$, $L^2 = 900$, $Re_{\mathcal{L}} = 1\times10^4$ for **a** $Wi_{\mathcal{L}} = 0.2$, $\delta_{(x/\mathcal{L}=1)}/\mathcal{L} = 0.03736$ **b** $Wi_{\mathcal{L}} = 0.4$, $\delta_{(x/\mathcal{L}=1)}/\mathcal{L} = 0.03701$

To verify the local approximate solution and assess its limit of validity in terms of the individual conformation tensor components, transverse profiles of C_{xy}, C_{yy}, C_{zz}, and C_{xx} are plotted and compared in Fig. 6 with the corresponding RheoFoam results. The data pertain to two different locations ($x/\mathcal{L} = 0.2$ and 1) and four different flow conditions ($Wi_{\mathcal{L}} = 0.1, 0.2, 0.3, 0.4$), in order to encompass a wide range of Wi_x. For $Wi_{\mathcal{L}} = 0.1$, the agreement is particularly good and for $Wi_{\mathcal{L}} = 0.2$ the accuracy of solution is acceptable. Further increasing $Wi_{\mathcal{L}}$ to 0.3 and 0.4 shows discrepancies between the profiles of the simplified theory and the predicted RheoFoam simulations, in particular for the highest Wi_x profiles showing that the conformation tensor components are the most sensitive quantities to flow elasticity. Such discrepancies appear both in the large positive peak values of C_{xx}, C_{xy} and negative peak values of C_{zz} appearing close to the centerline of the mixing layer, at $-0.4 \leq y/\delta \leq 0.4$. Similarly, the simplified theory is also unable to accurately follow the quick variations of the profiles of C_{yy} around 1 at the centerline.

Decreasing Wi_x by going downstream reduces the discrepancies and the behavior exhibited by the RheoFoam simulation is well described by the semi-analytical solution at $Wi_x = 0.2$, whereas at $Wi_x = 0.3$ the RheoFoam profiles show the appearance of local peaks that are not so well described by the approximate solution. Therefore, one may conclude that the critical value of Wi_x that marks the upper limit of validity of the semi-analytical solution lies between 0.2 and 0.3.

In this shear flow the mixing layer thickness is a more adequate length scale to define the Reynolds and Weissenberg numbers than x, but δ is part of the solution making it more difficult to quantify a priori, hence the use of Re_x and Wi_x instead of $\mathrm{Re}_\delta = \frac{U_1\delta,}{\nu_0}$, and $Wi_\delta = \frac{\lambda U_1}{\delta}$. As discussed by Parvar et al. [30] for boundary layer flows, this may raise questions as to what are low and high values of elasticity, and in particular whether the semi-approximate solution is only limited to low elasticity. For an appropriate assessment of the magnitudes of Wi_x and Wi_δ, Fig. 7 plots the variations of both quantities for two mixing layers showing that Wi_δ is at least one order of magnitude higher than Wi_x and that for the cases in Figs. 4 and 6 where $0.4 < Wi_x < 2.0$, one gets $1.5 < Wi_\delta < 12$, i.e., that the critical value of $0.2 < Wi_x < 0.3$ is well in excess of 1 if cast in terms of Wi_δ.

Finally, it is worth comparing the computational cost of the semi-analytical solutions and of the RheoFoam simulations. The latter were performed by a computer equipped with an Intel Xeon E5 processor with 12 MB L3 cache and Turbo Boost up to 3.9 GHz, with parallel processing using its 6 computer cores. The computational time was 4.0 h, however, for the semi-analytical solutions the same computer took about one second using only one core.

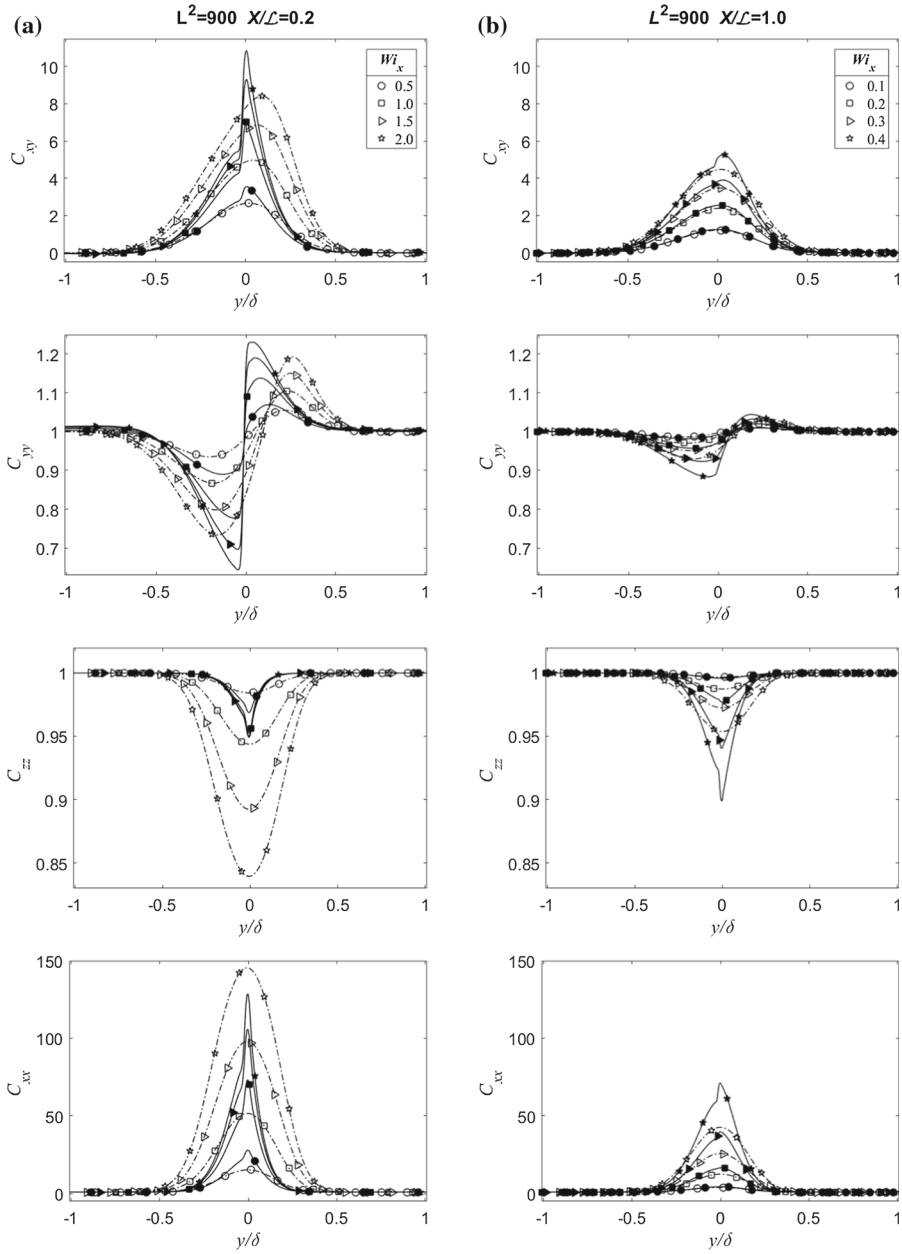

Fig. 6 Comparison between transverse profiles of conformation tensor components $C_{xy}, C_{yy}, C_{zz}, C_{xx}$ from present solution (dash dotted lines and open symbols) and RheoFoam simulations (solid lines and closed symbols) for $\beta_p = 0.1$, $L^2 = 900$, $Re_{\mathcal{L}} = 1 \times 10^4$, and $Wi_{\mathcal{L}} = 0.1, 0.2, 0.3$, and 0.4 at **a** $x/\mathcal{L} = 0.2$, **b** $x/\mathcal{L} = 1$

5.2.2 Velocity field and mixing layer thickness

The dependence of the normalized transverse profiles of streamwise and cross-stream velocity component velocities on fluid characteristics, at two different locations in the self-similar region (in the Newtonian fluid perspective), are shown in Fig. 8a and b. By normalizing the transverse coordinate with the mixing layer thickness, and the cross-stream velocity component velocity with the Reynolds number, unique profiles are obtained for u and v at

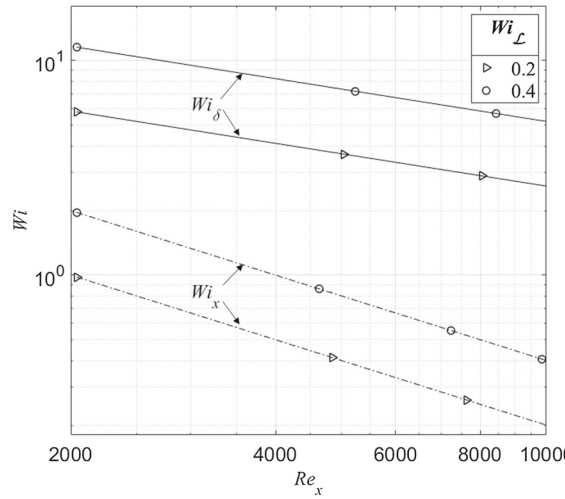

Fig. 7 Streamwise variation of Wi_x (dotted lines) and Wi_δ (solid lines) for two flows with $\beta_p = 0.1$, $L^2 = 900$, and $Re_{\mathcal{L}} = 10^4$. Lines are a guide to the eye

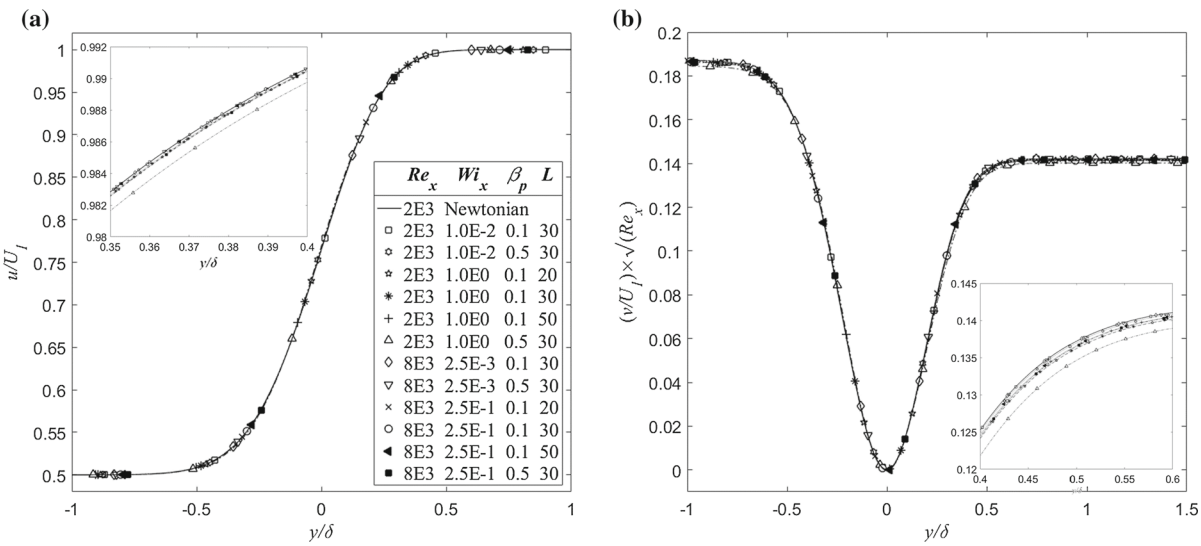

Fig. 8 Normalized transverse velocity profiles at $Re_x = 2000$ and 8000 as a function of Reynold number, Weissenberg number, viscosity ratio, and dumbbell extensibility for $\gamma = 0.5$: **a** u/U_1, **b** $v\sqrt{Re_x}/U_1$

low elasticity levels, which coincide with the Newtonian profiles. As elasticity levels are increased, small deviations from the low elasticity limit are observed for both components, as seen in the insets, thus showing the x-dependence of the viscoelastic similarity solution. These deviations are of the same magnitude as those previously seen for a planar laminar jet by Parvar et al. [28,29], but less intense than seen in a boundary layer by Parvar et al. [30], where the presence of the wall surface imposes higher deformation rates.

Figure 9 plots the streamwise variation of the velocity of the mixing layer at the inflection point shown by (u_c/U_1) for $\gamma = 0.5$, as a function of the independent dimensionless numbers, some of which were calculated at $x = \mathcal{L}$. At low elasticity levels, the velocity profiles collapse onto a single constant value identical to the Newtonian fluid case, $u_c/U_1 = 0.7652$. Increasing flow elasticity raises the velocity at the inflection point and makes it depend on x, with u_c/U_1 increasing towards the splitter plate, but these effects are small and for the tested cases the deviations are less than 1%. Notice that the local Weissenberg number increases on moving upstream on account of higher shear rates when the mixing layer is thinner.

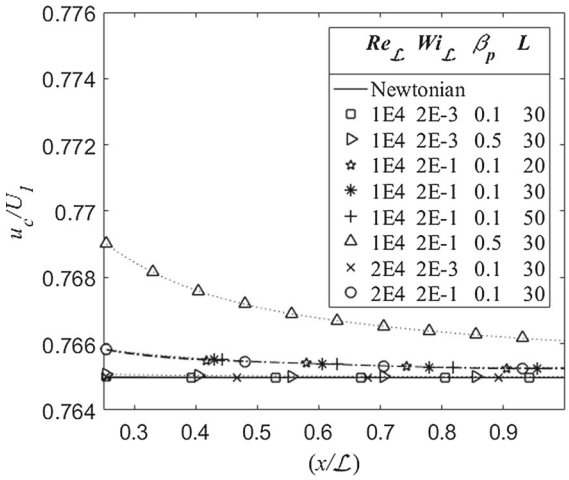

Fig. 9 Streamwise variation of normalized mixing layer centerline velocity (u_c/U_1) under various flow conditions for $\gamma = 0.5$. The solid line shows the Newtonian data $u_c/U_1 = 0.7652$, dashed lines are a guide to the eye

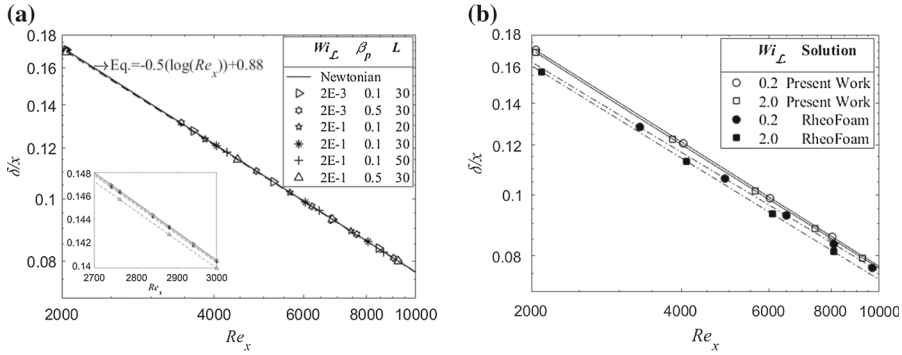

Fig. 10 Streamwise variation of the normalized mixing layer thickness (δ/x)under various flow conditions for $\gamma = 0.5$. The inset zooms in profiles for $2.7\times10^3 \leq Re_x \leq 3 \times 10^3$. Dashed lines are a guide to the eye

The streamwise variation of the normalized mixing layer thickness (δ/x) is plotted in Fig. 10a as a function of $Wi_{\mathcal{L}}$, β_p, and L. At low Weissenberg numbers δ/x data collapse to the Newtonian flow variation, as previously observed in the planar jet [28] and flat plate flows [30], but by increasing $Wi_{\mathcal{L}}$, β_p, or decreasing L, the mixing layer thickness decreases. To assess the accuracy of our semi-analytical solution in predicting normalized mixing layer thickness (δ/x), we compare with Rheofoam results for $Wi_{\mathcal{L}} = 0.2$ and 2.0 in Fig. 10b. The former value is at the limit of validity of the semi-analytical solution and the latter is well beyond that range of validity. As shown, the accuracy of the predictions is acceptable with differences below 3% even for large Wi, because δ/x is directly calculated from the velocity profiles which are significantly less sensitive to variations in Wi than the conformation tensor components. It is worth to mention that we faced numerical instabilities while solving the third-order differential equation for $Wi_{\mathcal{L}} > 2$.

The corresponding streamwise variations of the displacement (δ^*/x) and momentum (θ/x) thicknesses are presented in Figs. 11a and 12a , respectively. As expected, when the elasticity levels are weak, both profiles follow closely the corresponding Newtonian laws, however, by increasing the elasticity levels both the dimensionless displacement thickness (δ^*/x) and the dimensionless momentum thickness (θ/x) decrease. In the corresponding comparisons with RheoFoam, shown in Figs. 11b and 12b, respectively, acceptable agreements are seen, with differences not exceeding 4% at the highest Wi numbers. Again, these comparisons pertain to cases at the limit of validity of the semi-analytical solution, and beyond that limit.

The ratio δ^*/θ defines the shape factor (H) that is plotted in Fig. 13. Again, at low elasticity levels H collapses to the Newtonian value ($H = 1.633$), but it increases only very slightly with elasticity. For all quantities notice

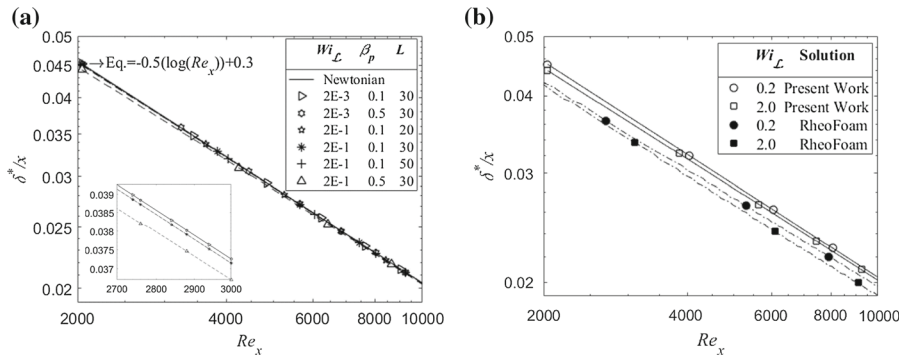

Fig. 11 Streamwise variation of the normalized displacement thickness (δ^*/x) under various flow conditions for $\gamma = 0.5$. The inset zooms in on profiles for $2.7\times10^3 \leq \mathrm{Re}_x \leq 3 \times 10^3$. Dashed lines are a guide to the eye

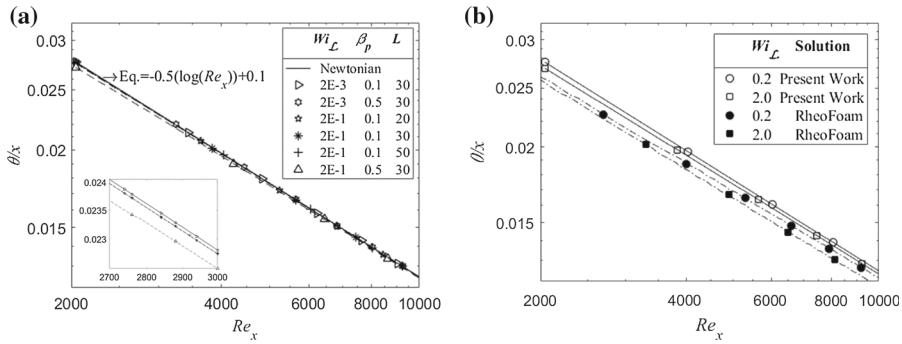

Fig. 12 Streamwise variation of the normalized momentum thickness (θ/x) under various flow conditions for $\gamma = 0.5$. The inset zooms in on profiles for $2.7 \times 10^3 \leq \mathrm{Re}_x \leq 3 \times 10^3$. Dashed lines are a guide to the eye

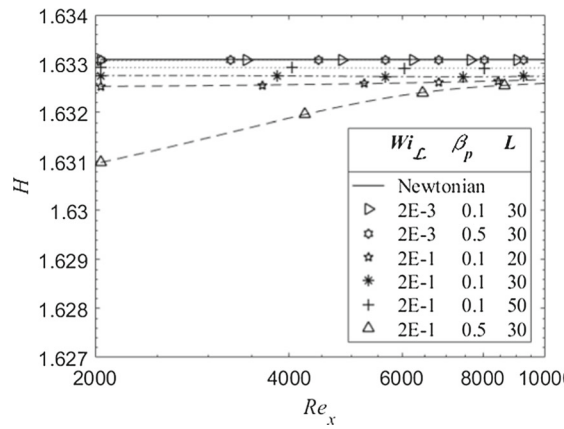

Fig. 13 Streamwise variation of the shape factor H for $\gamma = 0.5$ as a function of dimensionless flow and fluid characteristics. Dashed lines are a guide to the eye

that on moving downstream the curves approach the low elasticity asymptote because local values of Weissenberg number decrease.

5.2.3 Conformation and stress tensors

The corresponding profiles of the conformation and stress tensor quantities are presented and discussed here. Figure 14a–d plots the streamwise variations of the maximum value of the polymer stress components normalized by their corresponding values at $x/\mathcal{L} = 0.2$. These profiles exhibit linear variations in log–log coordinates, according to

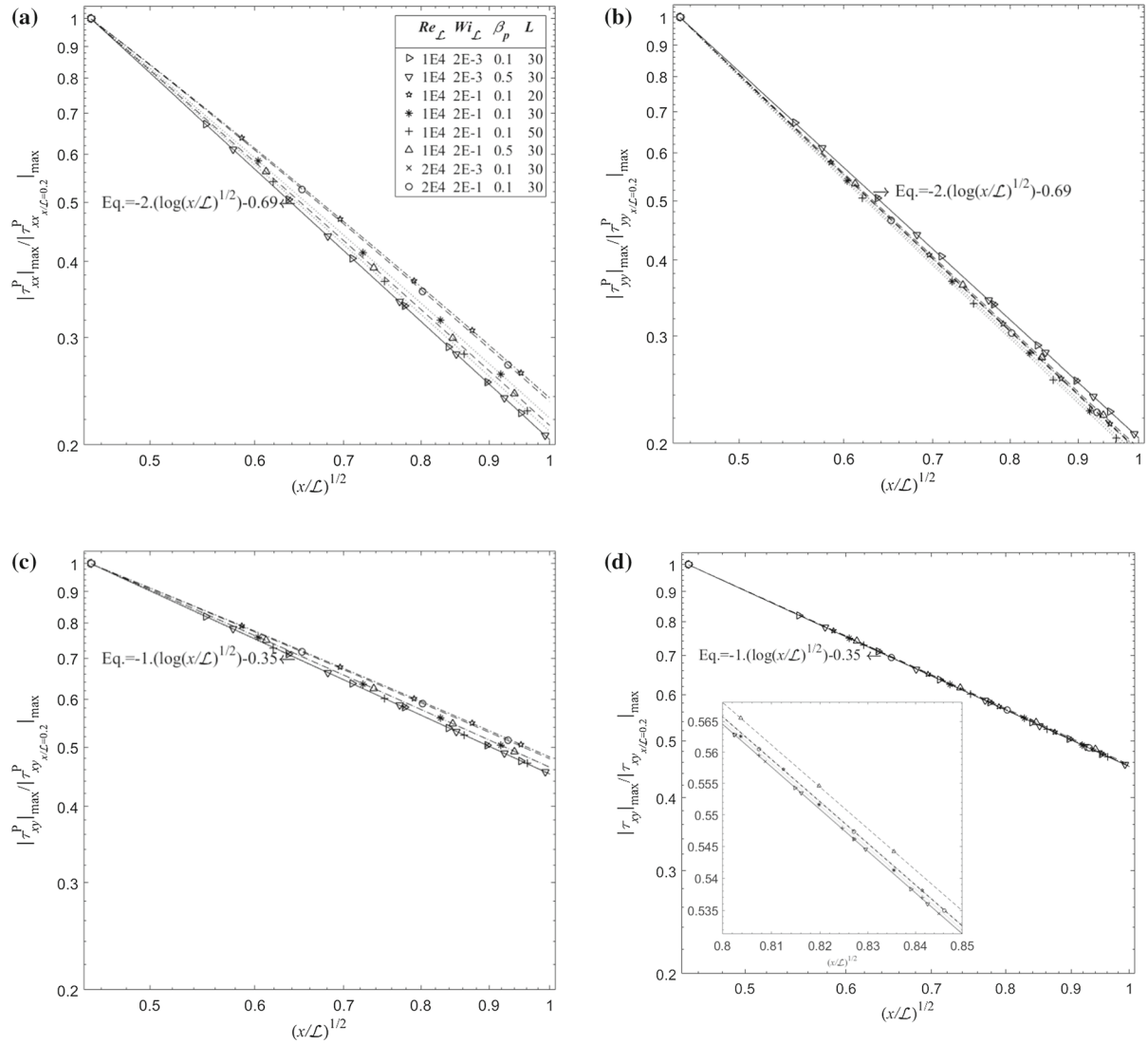

Fig. 14 Streamwise variation of normalized peak values of the stress tensor components for various rheological properties: **a** τ^{p}_{xx}, **b** τ^{p}_{yy}, **c** τ^{p}_{xy}, **d** τ_{xy}. Lines are a guide to the eye with the solid line representing the low elasticity asymptote

Eq. (51), and a low elasticity asymptote, with the rates of decay of τ^{p}_{xx} and τ^{p}_{yy} being equal to 2, which is twice as fast as for the polymer (τ^{p}_{xy}) and total (τ_{xy}) shear stresses.

$$\log_{10}\frac{\left|\tau^{\mathrm{p}}_{ij}\right|_{\max}}{\left|\tau^{\mathrm{p}}_{ij}\right|_{\max@\frac{x}{\mathcal{L}}=0.2}} = m\log_{10}\left[\left(\frac{x}{\mathcal{L}}\right)^{1/2}\right] - b. \tag{51}$$

The location of those maximum stresses for τ^{p}_{yy} and τ_{xy} under various flow conditions are exhibited in Fig. 15a and b. The peak values of the total shear stress τ_{xy} always occur at the centerline of the mixing layer, whereas the maximum τ^{p}_{yy} occurs always far from the centerline and its transverse distance to the centerline increases on going downstream. It is worth mentioning that the peak values of τ^{p}_{xx} and τ^{p}_{xy} occur very close to the centerline, but not at the centerline, however, such profiles are not shown for conciseness.

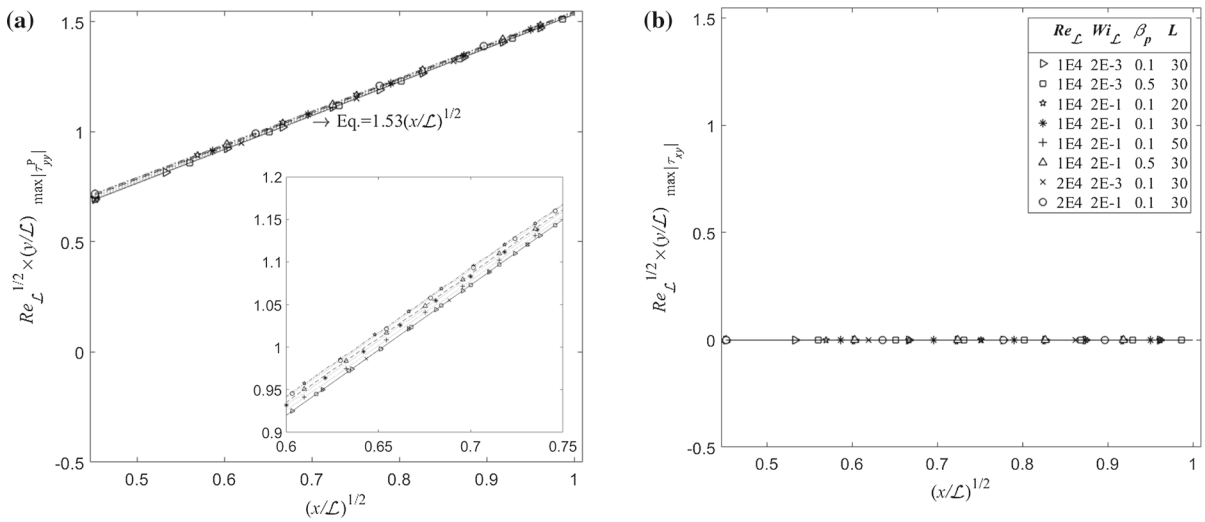

Fig. 15 The location of peak values of the stress tensor components for various rheological properties: **a** τ^{p}_{yy}, **b** τ_{xy}. Lines are a guide to the eye with the solid line representing the low elasticity asymptote

The ratios of maximum polymer over maximum solvent stresses $\left(\left|\tau^{\mathrm{p}}_{ij}\right|_{\max} / \left|\tau^{\mathrm{s}}_{ij}\right|_{\max}\right)$ are shown in Fig. 16. At low elasticity levels, these ratios behave similarly and equate to the ratio of viscosities $\nu^{\mathrm{p}}/\nu^{\mathrm{s}} = \beta_{\mathrm{p}}/(1-\beta_{\mathrm{p}}) = 1/9$ and 1 for $\beta_{\mathrm{p}} = 0.1$ and 0.5, respectively, because those stresses are essentially determined by the flow shear rate (in a rather complex way for the *yy* component) in the so-called first Newtonian plateau of shear viscosity. As flow elasticity increases this stress ratio decreases on account of shear-thinning behavior. However, the ratio $\left|\tau^{\mathrm{p}}_{xx}\right|_{\max} / \left|\tau^{\mathrm{s}}_{xx}\right|_{\max}$ behaves differently, being always above 1 and tending to increase significantly with elasticity since the numerator depends on the shear rate, whereas the denominator depends on the normal strain rate only.

Figure 17a–d shows again the x-dependence of the approximate self-similar characteristics of conformation tensor components: at low elasticity the behavior is actually independent of x, with a progressive deviation from the low elasticity asymptotic curves as *Wi* increases. The data are normalized by the corresponding local maximum values and covers a wide range of flow conditions pertaining to two different locations (represented as different values of Re_x).

Figure 18 shows the transverse variation of the total shear stress τ_{xy} normalized by the corresponding peak value. Similar to the profiles of the conformation tensor components, at low viscoelasticity levels the profiles collapse onto asymptotic curves, while increasing levels of viscoelasticity lead to progressive deviations from the asymptote. The deviation is small, however, because some of the variation in the polymer stress component is taken by the corresponding solvent stress, i.e., the total stress behaves almost as if it has a unique similar solution independent of x.

6 Conclusions

By utilizing boundary layer arguments, an order of magnitude analysis of the governing equations for the steady laminar mixing layer flow of FENE-P fluids was carried out leading to a set of simplified equations. The subsequent use of variables inspired by the similarity variables for the corresponding Newtonian solution is not able to provide a global approximate similarity solution, but only one that still depends on the streamwise coordinate, because of the viscoelastic constitutive equation. Nevertheless, under conditions of low elasticity, the normalized flow characteristics showed a behavior that depended only on the similarity variables and was independent of x, with kinematic quantities collapsing on the corresponding Newtonian self-similar data, and polymer-based quantities collapsing also onto single self-similar curves. Consequently, under these low elasticity flow conditions the ratio

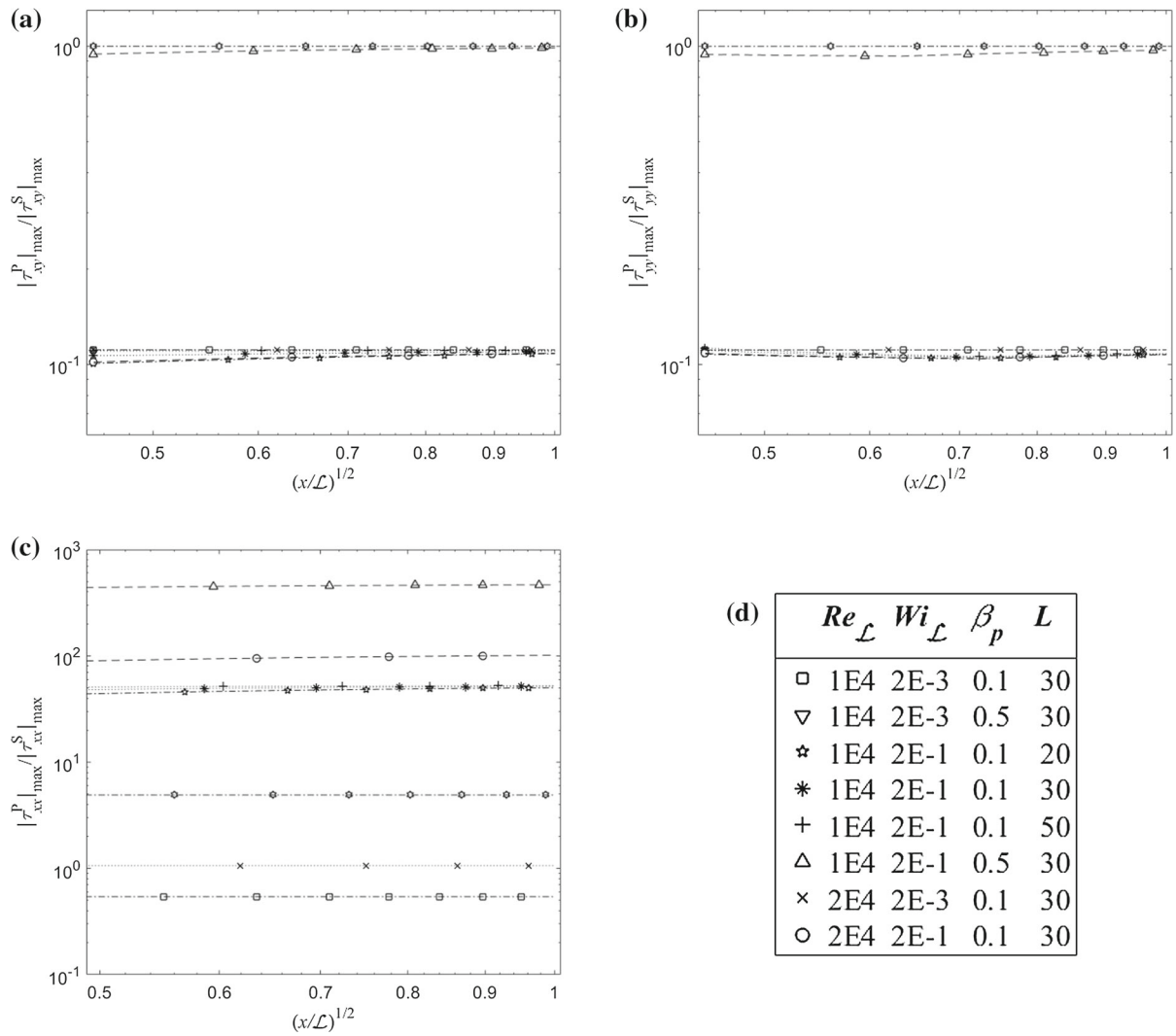

Fig. 16 The streamwise variation of the ratio of polymer stress (τ^{p}_{ij}) to solvent stress (τ^{s}_{ij}) at the mixing layer flow. **a** $\left|\tau^{\mathrm{p}}_{xy}\right|_{\max} / \left|\tau^{\mathrm{s}}_{xy}\right|_{\max}$, **b** $\left|\tau^{\mathrm{p}}_{yy}\right|_{\max} / \left|\tau^{\mathrm{s}}_{yy}\right|_{\max}$, **c** $\left|\tau^{\mathrm{p}}_{xx}\right|_{\max} / \left|\tau^{\mathrm{s}}_{xx}\right|_{\max}$, **d** Lines are a guide to the eye

of polymer over solvent stresses $\left(\left|\tau^{\mathrm{p}}_{xy}\right| / \left|\tau^{\mathrm{s}}_{xy}\right|\right.$ and $\left.\left|\tau^{\mathrm{p}}_{yy}\right| / \left|\tau^{\mathrm{s}}_{yy}\right|\right)$ were seen to be equal to the ratio of polymer to solvent kinematic viscosities. As elasticity levels increase, by taking on larger values of Wi_x and β_{p} and/or low values of L, there is a progressive deviation from the low Wi asymptote curves.

This work also reports on the variations of dimensionless boundary layer thickness (δ/x), displacement thickness (δ^*/x), and momentum thickness (θ/x). At low elasticity they follow the corresponding Newtonian data, but on increasing elasticity levels a decrease is observed. The variations of the peak values of the non-zero components of the conformation tensor and their spatial locations are also reported.

The semi-analytical solution can provide accurate results up to values of local Weissenberg number (Wi_x) of about 0.2, corresponding to values of Wi_δ well in excess of 1, which are well beyond the low elasticity assumption invoked initially. Beyond this flow condition, the local approximate similarity solution can still predict the normalized velocity profiles and the normalized evolution of the momentum, displacement, and mixing layer thicknesses within 5% of the RheoFoam solutions for $Wi_{\mathcal{L}} \leq 2$, $\beta_{\mathrm{p}} = 0.1$, and $L^2 = 900$. However, the approximate solution

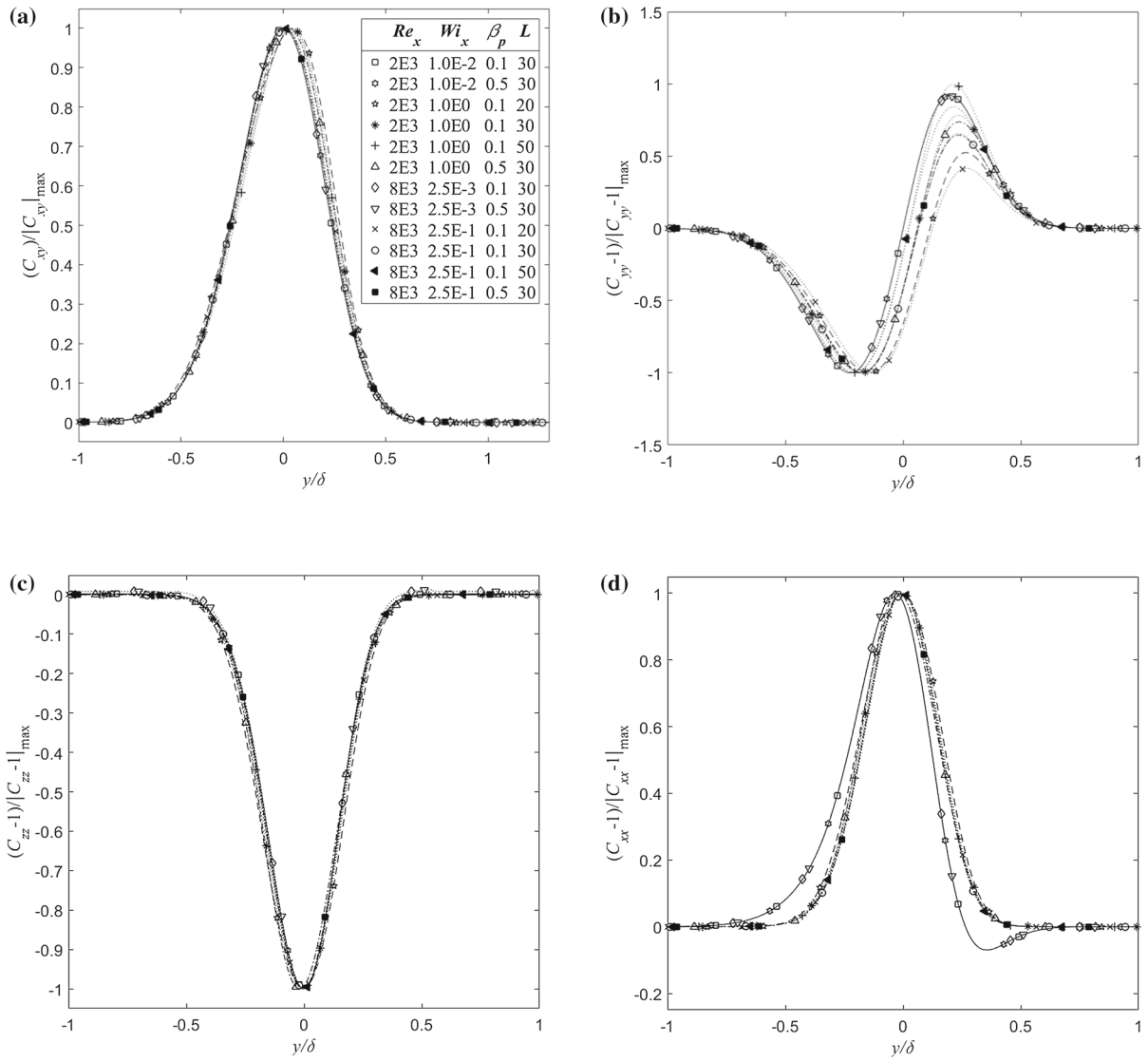

Fig. 17 Transverse profiles normalized components of the conformation tensor: **a** C_{xy}, **b** C_{yy}, **c** C_{zz}, **d** C_{xx}, for various rheological properties. Lines are a guide to the eye

prediction of the corresponding transverse variations of the conformation tensor components are subject to large errors, in particular around the centerline region ($-0.4 \leq y/\delta \leq 0.4$).

The computational cost of the approximate similarity semi-analytical solution is very low: using a single core it took about 1 s, which compares with 4 h for the corresponding RheoFoam simulation in a computer equipped with an Intel Xeon E5 processor with 12MB L3 cache and Turbo Boost up to 3.9 GHz, using its 6 computer cores through parallel processing.

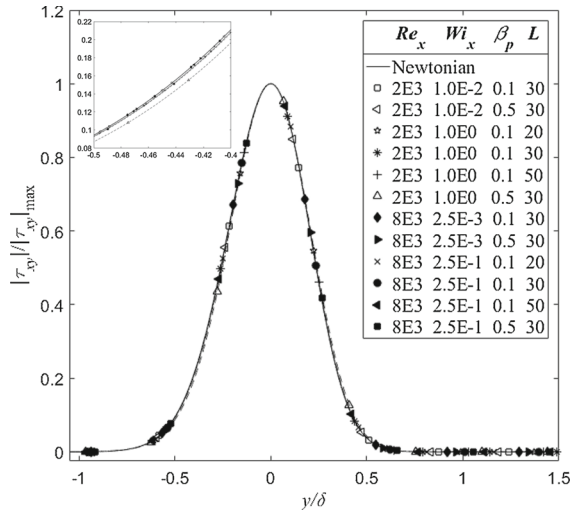

Fig. 18 Transverse profiles of normalized total shear stress τ_{xy} under various flow conditions for $\gamma = 0.5$. Dashed lines are a guide to the eye

Acknowledgements The authors acknowledge the financial support of project PTDC/EMS-ENE/2390/2014, POCI-01-0145-FEDER-016669 funded by Fundo Europeu de Desenvolvimento Regional, via COMPETE2020 - Programa Operacional Competitividade e Internacionalização (POCI) and Fundação para a Ciência e a Tecnologia. In addition S. P. and F. T. P. acknowledge financial support provided by Centro de Estudos de Fenómenos de Transporte through projects UIDB/ 00532/2020 and UIDP/00532/2020. C.B.S acknowledges Fundação para a Ciência e a Tecnologia (FCT) through IDMEC, under LAETA project UIDB/50022/2020.

References

1. White FM (2006) Viscous fluid flow, 3rd edn. McGraw Hill, New York
2. Schlichting H, Gersten K (1999) Boundary-layer theory, 8th revised and enlarged ed. McGraw Hill, New York
3. Pope SB (2000) Turbulent flows. Cambridge University Press, Cambridge
4. Prandtl L (1904) In: Verhandlungen des dritten internationalen Mathematiker-Kongresses in Heidelberg, Krazer A (1905) (ed) Teubner, Leipzig, Germany, 484. English trans. In: Ackroyd JAK, Axcell BP, Ruban AI (eds) Early developments of modern aerodynamics, 2001. Butterworth-Heinemann, Oxford
5. Blasius H (1908) Grenzschichten in Flüssigkeiten mit kleiner Reibung. Z Angew Math Phys 56:1–37
6. Birkhoff G, Zarantonello EH (1957) Jets, wakes and cavities. Academic Press, New York
7. Lessen M (1950) On stability of free laminar boundary layer between parallel streams. Report NACA-TR-979, NACA
8. Chapman DR (1950) Laminar mixing of a compressible fluid. Report NACA-TR-958, NACA
9. Kuethe AM (1933) Investigations of turbulent mixing regions. Thesis of Doctor of Philosophy, California Institute of Technology, Pasadena
10. Lock RC (1951) The velocity distribution in the laminar boundary layer between parallel streams. Q J Mech Appl Math 4(1):42–63
11. Nash JF (1962) Laminar mixing of a non-uniform stream with a fluid at rest. Ministry of Aviation Aeronautical Research Council. C. P, No, p 613
12. Ting L (1959) On the mixing of two parallel streams. J Math Phys 38(4):153–165
13. Klemp JB, Acrivos A (1972) A note on the laminar mixing of two uniform parallel semi-infinite streams. J Fluid Mech 55(1):25–30
14. Voropayev S, Smirnov S, Testik F (2003) On the case when steady converging/diverging flow of a non-Newtonian fluid in a round cone permits an exact solution. Mech Res Commun 31(4):477–482
15. Azaiez J, Homsy GM (2006) Linear stability of free shear flow of viscoelastic liquids. J Fluid Mech 268:37–69
16. Hinch EJ, Appendix E, Long-wave instability of a free shear layer of an Oldroyd-B fluid in Azaiez J, Homsy GM (1994) Linear stability of free shear flow of viscoelastic liquids. J Fluid Mech 268:37–69
17. Azaiez J, Homsy GM (1994) Numerical simulation of non-Newtonian free shear flows at high Reynolds numbers. J Non-Newtonian Fluid Mech 52:333–374
18. Bird RB, Armstrong RC, Hassager O (1987) Dynamics of polymeric liquids 1: fluid mechanics, 2nd edn. Wiley, New York
19. Bird RB, Curtiss CF, Armstrong RC, Hassager O (1987) Dynamics of polymeric fluids 2: kinetic theory, 2nd edn. Wiley, New York
20. Peterlin A (1961) Streaming birefringence of soft linear macromolecules with finite chain length. Polymer 2:257
21. Kumar S, Homsy GM (1999) Direct numerical simulation of hydrodynamic instabilities in two- and three-dimensional viscoelastic free shear layers. J Non-Newton Fluid Mech 83:249–276
22. Yu Z, Phan-Thien N (2004) Three-dimensional roll-up of a viscoelastic mixing layer. J Fluid Mech 500:29–53

23. Ray PK, Zaki TA (2014) Absolute instability in viscoelastic mixing layers. Phys Fluids 26:014103
24. Varshney A, Steinberg V (2018) Mixing layer instability and vorticity amplification in a creeping viscoelastic flow. Phys Rev Fluids 3:103303
25. Rajagopal KR, Gupta AS, Na TY (1983) A note on the Falkner–Skan flows of a non-Newtonian fluid. J Non Linear Mech 18(4):313–320
26. Olagunju DO (2006a) Local similarity solutions for boundary layer flow of a FENE-P fluid. Appl Math Comput 173:593–602
27. Olagunju DO (2006b) A self-similar solution for forced convection boundary layer flow of a FENE-P fluid. Appl Math Lett 19:432–436
28. Parvar S, Silva CB, Pinho FT (2020) Local similarity solution for steady laminar planar jet flow of viscoelastic FENE-P fluids. J Non-Newton Fluid Mech 279:104265
29. Parvar S, Silva CB, Pinho FT, (2021) Corrigendum to Local similarity solution for steady laminar planar jet flow of viscoelastic FENE-P fluids [J. Non-Newton Fluid Mech 279, (2020) 104265]. J Non-Newton Fluid Mech 281:104309
30. Parvar S, Silva CB, Pinho FT (2021) Revisiting the laminar boundary layer flow of viscoelastic FENE-P fluids. Phys Fluids 33(2):023103
31. Bird RB, Dotson PJ, Johnson NL (1980) Polymer solution rheology based on a finitely extensible bead-spring chain model. J Non-Newton Fluid Mech 7:213–235
32. Beris AN, Edwards BJ (1994) Thermodynamics of flowing systems with internal microstructure. Oxford Science Publication, New York
33. Vaithianathan T, Collins LR (2003) Numerical approach to simulating turbulent flow of a viscoelastic polymer solution. J Comput Phys 187:1–21
34. Valente PC, Silva CB, Pinho FT (2014) The effect of viscoelasticity on the turbulent kinetic energy cascade. J Fluid Mech 760:39–62
35. Li CF, Gupta VK, Sureshkumar R, Khomami B (2006) Turbulent channel flow of dilute polymeric solutions: drag reduction scaling and an eddy viscosity model. J Non-Newton Fluid Mech 139:177–189
36. Masoudian M, Pinho FT, Kim K, Sureshkumar R (2016) A RANS model for heat transfer reduction in viscoelastic turbulent flow. Int J Heat Mass Transf 100:332–346
37. Guimarães MC, Pimentel N, Pinho FT, Silva CB (2020) Direct numerical simulations of turbulent viscoelastic jets described by the FENE-P model. J Fluid Mech 899:A11
38. Parvar S, Silva CB, Pinho FT (2021) Large eddy simulations of turbulent planar jets of viscoelastic fluids. Phys Fluids 33:045110
39. Cebeci T, Bradshaw P (1984) Physical and computational aspects of convective heat transfer. Springer, Berlin
40. Sparrow EM, Quack H, Boerner CJ (1970) Local nonsimilarity boundary-layer solutions. AIAA J 8(11):1936–1942
41. Sparrow EM, Yu HS (1971) Local non-similarity thermal boundary-layer solutions. ASME J Heat Transf 93(4):328–334
42. Massoudi M (2001) Local non-similarity solutions for the flow of a non-Newtonian fluid over a wedge. Int J Non Linear Mech 36(6):961–976
43. Edberg L (2016) Introduction to computation and modeling for differential equations, 2nd edn. Wiley, Hoboken, New Jersey
44. Madureira A (1948) Lessons in algebra and analytical geometry, vol 1– Algebra, 2nd edn. Porto Editora, Porto, Portugal **(in Portuguese)**
45. Press WH, Teukolsky SA, Vetterling WT, Flannery BP (2007) Numerical recipes: the art of scientific computing, 3rd edn. Cambridge University Press, New York
46. Birkhoff G, MacLane S (1998) A survey of modern algebra (Akp classics), 5th edn. A K Peters/CRC Press, Boca Raton
47. Alston TM, Cohen IM (1992) Decay of a laminar shear layer. Phys Fluids A 4:2690
48. Alves MA, Oliveira PJ, Pinho FT (2003) A convergent and universally bounded interpolation scheme for the treatment of advection. Int J Numer Methods Fluids 41:47–75
49. Pimenta F, Alves MA (2016) rheoTool. https://github.com/fppimental/rheotool
50. Pimenta F, Alves M (2017) Stabilization of an open-source finite-volume solver for viscoelastic fluid flows. J Non-Newton Fluid Mech 239:85–104
51. Dimotakis PE (2000) The mixing transition in turbulent flows. J Fluid Mech 409:69–98